Pro Gradu

Functionalized carbon nanotube for next generation biosensor

Shao Dongkai

November 6, 2013

UNIVERSITY OF JYVÄSKYLÄ

DEPARTMENT OF PHYSICS

NANOSCIENCE CENTER

Preface

The work reported in this M.Sc.Thesis (Pro Gradu) has been done between September 2012 and September 2013 in the Nanoscience Center of the University of Jyväskylä.

First, I would like to give my sincere thanks to Prof.Markus Ahlskog, who led me to the carbon nanomaterials and biophysics research fields and gave me a lot of useful guidance and warm encouragement.

Biophysics research is such an exciting and complicated research area, and without yours' help, Dr Andreas Johansson, Olli Herranen, Matti Hokkanen, Yotprayoonsak Peerapong, Dr.Kimmo Kinnunen, Tarmo Suppula, Jarno Alaraudanjoki Professor.Janne Ihalainen, Professor.Hannu Häkkinen and Riitta-Liisa Kuittinen,this work could have been more difficult.

I greatly appreciate all the people who were involved in this research programme on Programmable materials by the Academy of Finland, Dr.Jussi Toppari, Kosti Tapio, Dr.Vesa Hytönen (University of Tampere), Professor.IIpo Vattulainen (Tampere University of Technology) and bachelor student Hannu Pasanen, I feel so appreciated.

And finally, thank you all the Chinese personnel who work in the Nanoscience center, your company makes my life in Finland have some Chinese taste.

This research is supported by the Academy of Finland and the Department of Physics at the University of Jyväskylä.

Jyväskylä, November 6, 2013

Shao Dongkai

Introduction

A biosensor based on a carbon nanotube, due to its well-defined nanoscale dimension and unique molecular structure, can be used to bridge linking biomolecules to macro/micro- solid-state devices. It has been a hot research field for the last decades. It is believed that this miniature sensor device could be the crucial step for the next generation "point-of-care" biosensor, and finally used in clinical practice.

In this thesis, the contents are in general divided into three parts- a theoretical part, an experimental part and an appendix part. In the theory part, I mainly introduced some basic concepts of a carbon nanotube based biosensor, like target protein (Chapter 1), carbon nanotube (Chapter 2), the detection of gold particles (Chapter 3) and two chapters' technology issues, like characteristic of biosensor (Chapter 4) and surface functionalization (Chapter 5).

For experimental and discussion part, the contents naturally can be split as two sections. From Chapter 6 to Chapter 7, I mainly show the experiments associated with individual parts of one carbon nanotube based biosensor with normal nanotechnology characterizing facilities (optical microscope, AFM, SEM etc). Based on these experiment results, in Chapter 8, I will try to present one practical carbon nanotube sensor on silicon surface. The technology used in this core experiment include: microfabrication, carbon nanotube dispersion, single carbon nanotube location, carbon nanotube functionalization, chimeric avidin covalent immobilization and single protein detection. It maybe not necessary for experienced scientists or researchers to read the material in the order presented here. Some people may find it is easier to read the Chapter 8 first and then go to the technology details in Chapter 6 or Chapter 7.

Some useful parameters of facilities used in these experiments and one chapter about supramolecular chemistry are listed in the Appendix.

Contents

Part I

Material

Chapter 1

Target proteins

1.1 Chemical components of protein and four level protein structure

Proteins, from Greek word "proteios (meaning "first place")", account for more than 50 percent of the dry mass of most cells[1]. Based on their functionalization in organisms, proteins can be divided into enzymatic protein, structural protein, storage protein, transport protein hormonal protein, receptor proteins, contractile and motor proteins and defensive protein. In clinic, the measurement of certain proteins in blood or urine is widely used, as direct evidence of certain disease or health disorder[2, 3].

From a chemical view, all proteins in human body are constructed from a set of 20 different amino acids (see Figure. 1.1(A)). These amino acids are composed of the identical amine (-NH_2), carboxylic acid (-COOH) functional groups, and a variable side chain (-R) group. In eukaryotic cells, each amino acids is specific translated from three nucleotide bases on messenger ribonucleic acid (mRNA) in ribosomes. Artificially modification one protein's amino sequence is possible in laboratory by genetic engineering at this stage.

Translated amino acids join with each other and form a sequence under a dehydration reaction mechanism (one amine group and one carboxylic acid groups forms one peptide bond). This amino acid sequence is called the protein's primary structure. In this sequence, the unbounded amine group and carboxylic acid group at the ends of the backbone peptide chain are called N-terminus and C-terminus. The primary structure of protein will continue to coil or to fold to form either a "α helix" or a " β sheet" (see Figure. 1.1(B)), due to hydrogen bonding between main-chain peptide groups, which is called the protein's secondary structure. Moreover, due to the formation of disulfide bridges, and the tendency of the hydrophobic parts under the weak hydrophobic force to hide into the core region, one obtains the protein's tertiary structure. And finally, some proteins consists of more than one polypeptide chain, from which arises the qua-

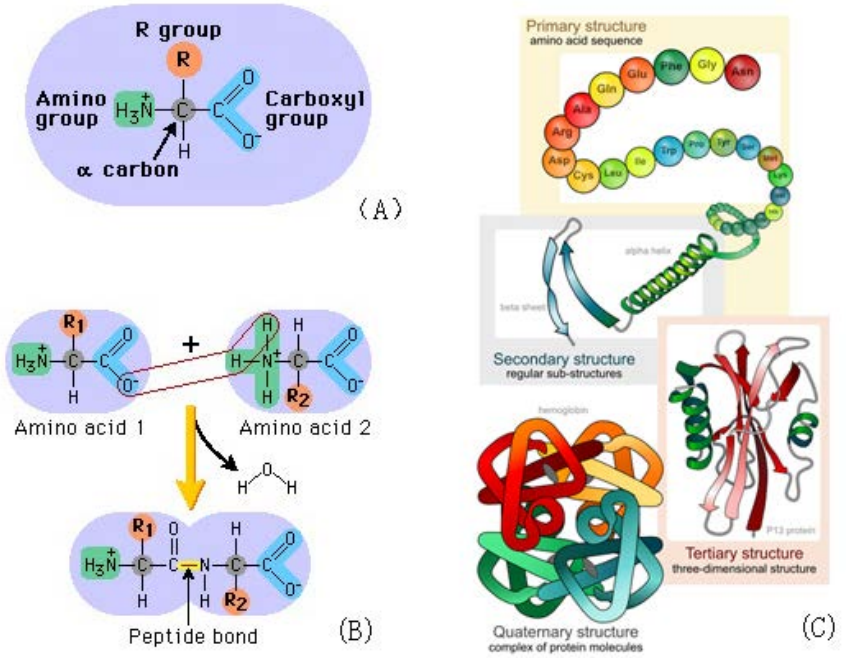

Figure 1.1: (A), Components of an amino acid; (B) The peptide Bond formation by two amino acids; (C) The four level structure of protein, from primary to quaternary structure.[Pearson BioCoach Activity and Wikipedia]

ternary structure (see Figure.1.1(C)).

1.2 Avidin, streptavidin and chimeric avidin

1.2.1 Avidin

Avidin is a glycoprotein found in the egg white and tissues of birds, reptiles and amphibians[4]. It contains four identical subunits, consisting of 128 amino acids, having a combined mass of 67,000 - 68,000 Dalton. The extent of glycosylation on avidin is high, which gives it a relatively high nonspecific binding property.

In biophysics, avidin is famous for its high affinity to biotin (see Section.1.3), that each subunit can bind one molecule of, with a dissociation constant of $K_D = 10^{-15}M$. This property makes it one of the strongest known non-covalent bonding, and widely used as crosslinker. The isoelectric point for avidin (the pH at which a particular molecule or surface carries no net electrical charge) is 10.5. In neutral buffer, avidin is positively charged.

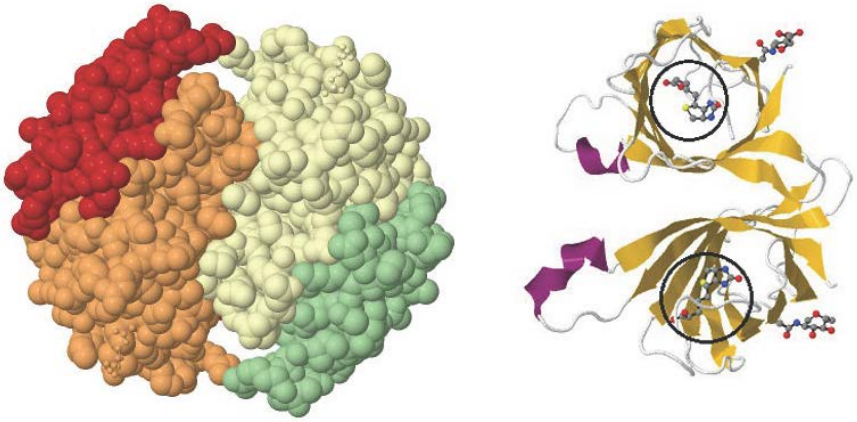

Figure 1.2: (The three dimensional structure of avidin and biotin. The space filling model (left) shows the structure of four identical subunits. The ribbon diagram (right) displays asymmetric unit two subunits of the eight strands of the β barrel structure and biotin molecules (in the black ovals) in the binding pockets. The images were generated from RCSB Protein Data Bank entries 2AVI[5].

1.2.2 Streptavidin

Streptavidin is a tetrameric protein, which is isolated from streptomyces avidinii[6]. Previous research shows that it has only 30 percent sequence identity to avidin, but their secondary, tertiary and quaternary structure (see Fig.1.2 and Fig.1.3) are quite similar. Comparing with avidin, streptavidin has at least two advantages when choosing a biotin-conjugate binder. The first difference is that streptavidin's carbohydrate component is lower than avidin, which could in principle lower the possibility of non-specific binding due to pure hydrophobic interaction. The second difference is that streptavidin has a mildly acidic isoelectric point of 5.5, and it has little net charge in neutral buffers.

1.2.3 Chimeric avidin

Chimeric avidin was first assembled in 2004 by Vesa Hytönen et al[8] using E.coli. The name of "chimeric" comes from its particular stability against harsh chemical conditions[9]. The molecular mass of chimeric avidin is 52.6 kD and the enthalpy of chimeric avidin-biotin binding -112.6kJ/mol[10]. In this Master's Thesis research, chimeric avidin is the main target analyze protein.

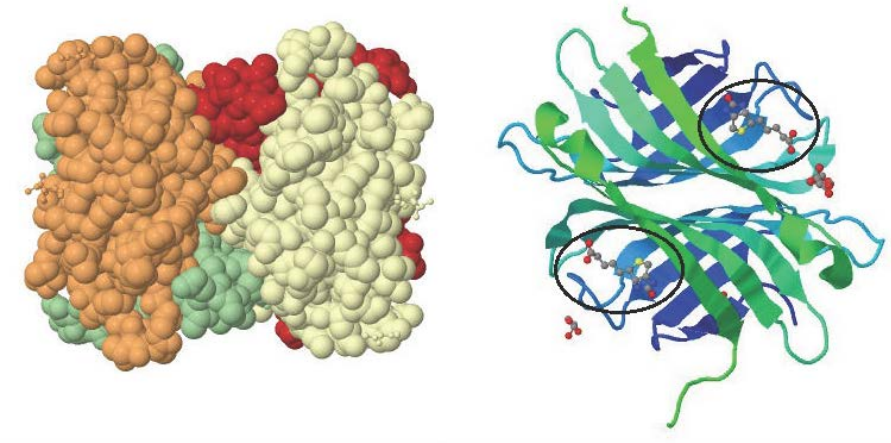

Figure 1.3: (The three dimensional structure of streptavidin and biotin. The space filling model (left) shows the structure of four identical subunits. The ribbon diagram (right) displays asymmetric unit two subunits of the predominant β barrel structure and biotin molecules (in the black ovals) in the binding pockets. The images were generated from RCSB Protein Data Bank entries 3RY2[7].

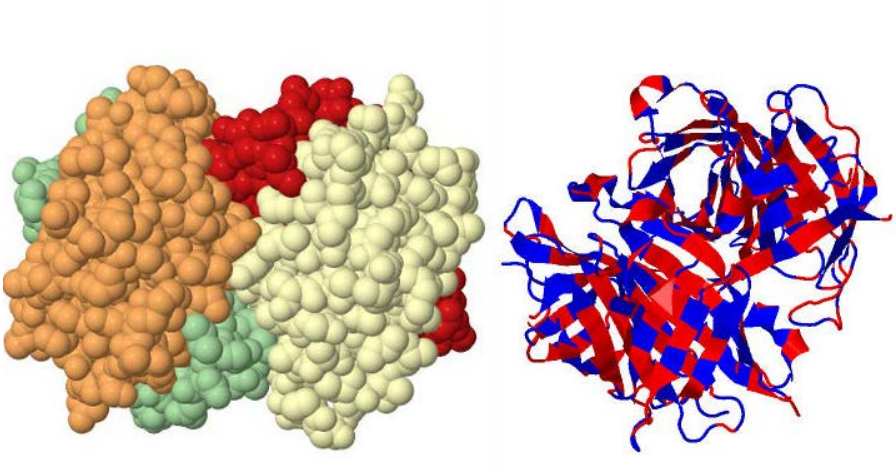

Figure 1.4: (The three dimensional structure of streptavidin and biotin. The space filling model (left) shows the structure of four identical subunits. The hydrophobicity figure (right) displays the affinity of amino sequence to water(red means hydrophobic and blue means hydrophilic). The images were generated from RCSB Protein Data Bank entries 3MM0[10].

1.3 Biotin and biotinylation

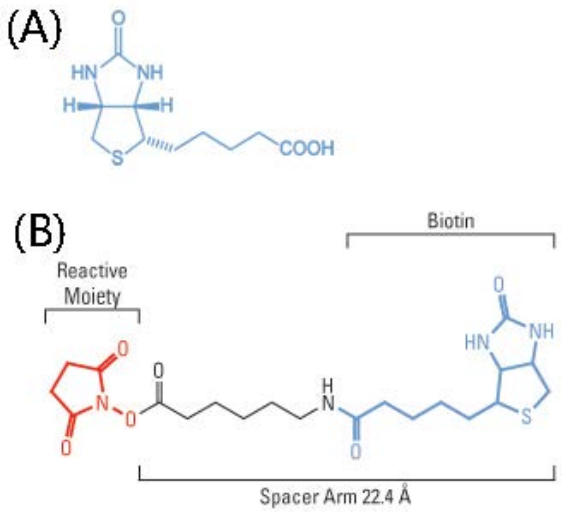

Figure 1.5: (A), Molecule structure of biotin; (B) Biotin-LC-NHS conjugation, where biotin molecule (blue) is conjugated to a reactive group (red) either directly or with additional chemical spacer (black). From Thermo Scientific [4]

Biotin (also known as Vitamin H, see Fig.1.5(A)), is an essential coenzyme required by all forms of life. It can be synthesized by plants, most bacteria and some fungi[11]. In cells, biotin is involved as an enzyme in the synthesis of fatty acids, isoleucine and in gluconeogensis etc. Lack of biotin (biotin deficiency) is really rare among heathy people, due to its low daily requirement. So biotin research usually has no significant pharmacological use [Wikipedia].

But in biophysics, biotin is widely used as cross linker or for molecule modification (biotinylation) for the following reasons[12]. Firstly, the interaction between biotin and avidin has an extremely high affinity (Ka=$10^{15}M^{-1}$). Once the binding formed, it is unlikely to be affected by extreme pH, temperature conditions or by adding organic solvents and other denaturing agents[13–19]. In addition, biotin is a comparatively small molecule, which does not interference with its targeting molecule's property. Thirdly, biotin has a valeric acid side chain (Fig.1.5(A)) which can be used for further conjugation or modification of its spacer arm(Fig.1.5(B)) . Some commercial reactive moieties based on biotin and their properties are listed in the Table 1.1.

Table 1.1: Biotinylation reagent and their target groups

Target functional groups	Biotinylation reagents	Properties
Primary amine	NHS-PEC-biotin	PEG spacer arm increases solubility
	Sulfo-NHS-biotin	Reacts with primary at ph 7-9, water soluble
	TFP-PEG3-biotin	TFP ester reacts with primary and secondary amines, water sobulbe
Carboxyl and carboyl reactive groups	Amine-PEG2-biotin	water soluble
	Hydrazide-biotin	must be dissolved in DMSO
	Alkoxyamine-PEG4-biotin	
Sulfhydral groups	BMCC-biotin	water soluble analog of biotin-LC-hydrazide
	locdoacetyl-LC-bioton	React with sulfhydryl groups at neutral ph
	HPDP-bioton	reacts with sulfhydryl groups at pH 6-9

Chapter 2

The Carbon nanotube

2.1 Discovery history

Systemical research of carbon nanotube began from 1991 after Sumio Iijima and Toshinari Ichihashi's famous paper in Nature[20, 21]. But the first observation of this carbon cylindrical structure can be found much earlier dating back to 1950's[22, 23]. After 20 years of development, carbon nanotubes' have been widely researched in many research areas. Some promising research areas include structural materials (such as tennis racket, ice hockey stick, or even future's space elevator), ultra fine tips for scanning probe microscopy[24], nanoelectronic devices, cancer detection and therapy[25, 26], drug delivery[26], field effect sensors [27] etc.

2.2 Carbon sp^2 orbital hybridization and Van der Waals force in carbon nanotube bundles

A carbon atom has totally six electrons, two of them called core electrons are in $1s$ orbitals, which do not participate any chemical reaction. The other four electrons (valence electrons) occupied in $2s2p$ orbitals. From the atom's energy level configuration, these four electrons should arrange in $2s^2 2p_z^1 2p_x^1$ orbitals. But in practice, these two shells ($2s$ and $2p$) are usually mixable and form so called sp, sp_2 and sp_3 hybridized orbitals.

For carbon nanotube and graphene, most carbon atoms have the electron configuration of $1s^2 2sp_2^1 2sp_2^1 2sp_2^1 2p_y^1$ (See Figure.2.1(A)).This electron configuration is so called $2sp_2$ hybridization, which means one electron in $2s$ orbital gaining energy and hybridizing with two electrons in $2p$ orbitals. sp_2 hybridized electrons have $\frac{1}{3}$ $2s$ and $\frac{2}{3}$ $2p$ electrons' properties.

When two sp_2 hybridized carbon atoms get close to each other, they can form a strong

σ bond by $sp_2 - sp_2$ overlap in their nodal plane. The unhybridized p_y orbitals on each carbon will interact by sideways overlap and form a π bond[28](see Fig.2.1(C)). One interesting chemical property of carbon nanotubes compared with pure graphite surface or graphene, is that there exist some partial sp_3 hybridized carbon atoms at the "end" or "cap" area of the carbon nanotube, due to its curvature. This phenomenon is called "$\sigma - \pi$ rehybridization"(see Fig.2.1(B)). Rehybridized carbons are more likely to undergo modification in chemical functionalization processes.

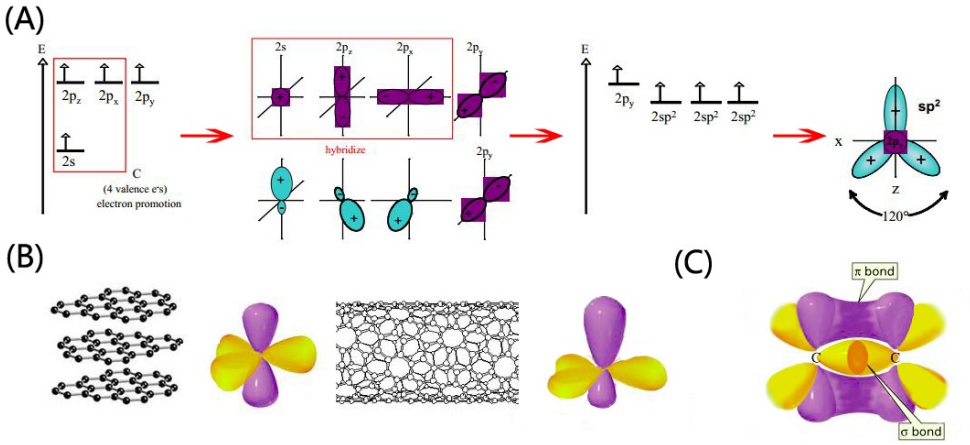

Figure 2.1: (A),sp2 hybrid orbitals in a carbon atom [MIT opencourse] (B), Crystal structures of graphite and nanotube and $\sigma - \pi$ rehybridization sp_2 orbitals due to the curvature (C), carbon double bonds between two carbon atoms

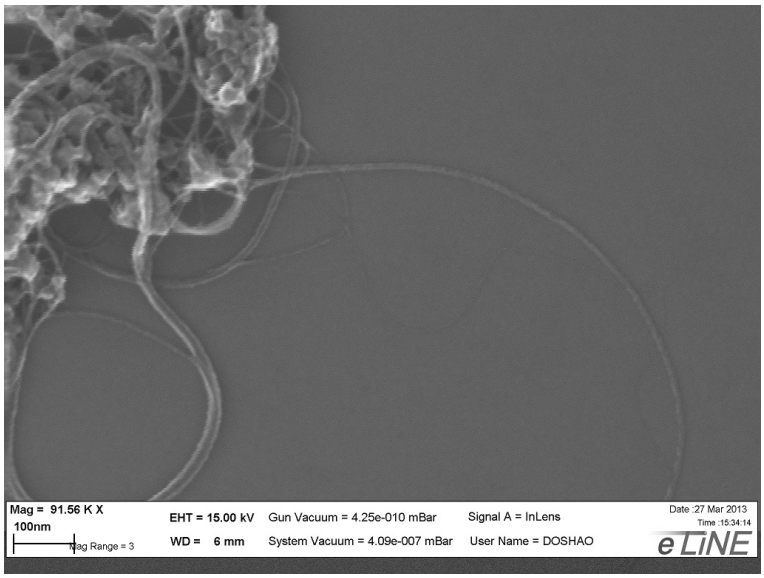

Figure 2.2: SEM image of Karlsruhe single walled carbon nanotubes's bundles, size bar=100 nm

Beside these covalent bonds between neighboring carbon atoms in CNT, weak interac-

tion, such as van der Waals force and $\pi - \pi$ stacking make CNT easily aggregate into "ropes" or "bundles"(see Fig.2.2). How to disperse these aggregated CNT polymers is still a very hot research area in CNT functionalization[29].

2.3 Physical properties of pristine carbon nanotube

2.3.1 Crystal structure and electronic band structure of graphene

A Single-walled carbon nanotube is usually regarded as one rolling sheet of graphene, while a multi-walled carbon nanotube can be treated as multiple concentric single-walled carbon nanotubes. Thus it will be greatly helpful to gain some knowledge about graphene before we explore carbon nanotubes.

Without considering curvature, the lattice of CNT and graphene are similar honeycomb hexagonal network (Fig.2.3(C)). In solid state physics, this structure belongs to the triangular Bravais lattice. Two neighboring carbon atoms (see Fig.2.3 (A), sublattice A and sublattice B), with distance of 0.142 nm, compose its Bravais lattice. The two Bravais lattice vectors satisfies the Equation.2.1.

$$a_{1\ or\ 2} = \frac{a}{2}(\pm 1, \sqrt{3}) \tag{2.1}$$

From calculation, the area of one unit cell (orange colored rhombus in Figure 2.3(A)) is $A_{uc} = \sqrt{3}a^2 = 5.25\mathring{A}^2$.

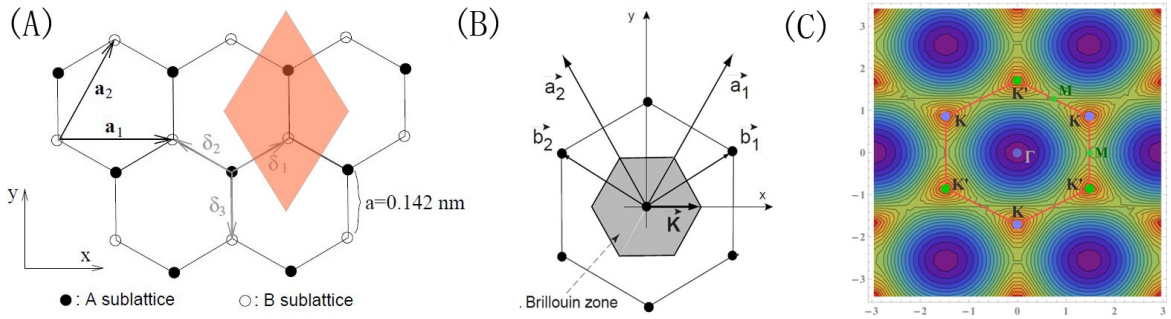

Figure 2.3: (A), Honeycomb lattice of graphene. The neighboring two carbon atoms (one black dot and one white dot) compose of one unit cell. Vectors a_1 and a_2 are basis vectors of triangular Bravais lattice[30]. (B), Reciprocal lattice of graphene with 1st Brillouin zone (shaded), $\vec{b_1}$ and $\vec{b_2}$ are the primitive lattice vectors[31].(C), Extended reciprocal lattice of graphene. The region inside red color lines is the first Brillouin zone (BZ), with its center Γ and two inequivalent corners K (purple dots) and K' (green dots). M are the saddle of neighboring two K and K' points. In this picture are totally two Brillouin zones. Figure from Vladimir Gavryushin Mathematica modeling.

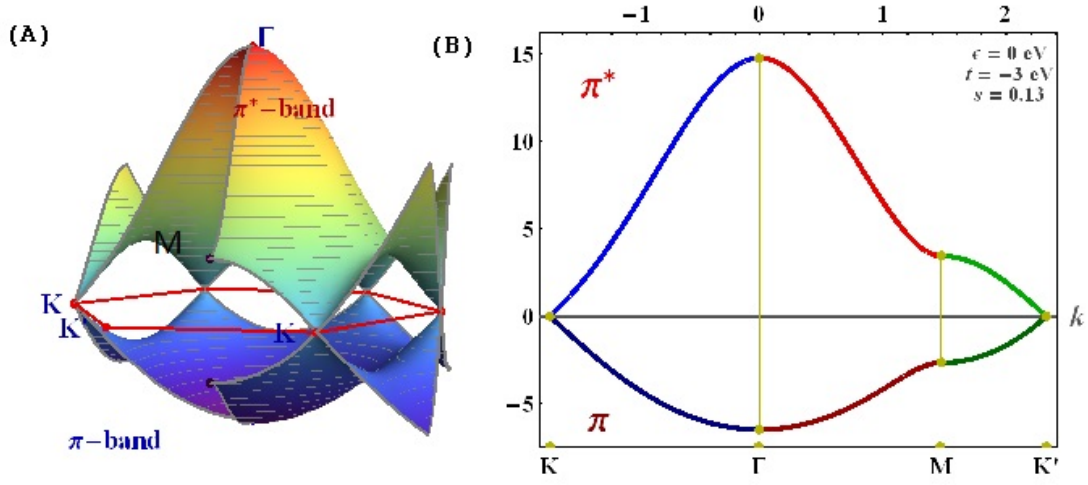

Figure 2.4: (A) Energy dispersion within tight-binding approximation. The upper valence band is π band, and the upper structure is π^* band. The Fermi level is situated at the points where the π band touches the π^* band. Energy dispersion is a function of the wave vector components of k_x and k_y; (B) Cut through the energy dispersion along characteristic lines. From Vladimir Gavryushin Mathematica modeling.

The reciprocal lattice of graphene lattices (Figure.2.3(B) and (C)) satisfy Equation.2.2:

$$b_{1\ or\ 2} = \frac{b}{2}(\pm\sqrt{2}, 1) \tag{2.2}$$

The six points (K and K', see, Fig.2.3(C)) at the corners of first Brillouin zone can be separated into two inequivalent groups with coordinates

$$K = \frac{4\pi}{3a}(-1, 0)\ and\ K' = \frac{4\pi}{3a}(1, 0) \tag{2.3}$$

In a simplest mode of tight-binding model of a graphene honeycomb (see Figure.2.3.1), the energy dispersion relation of graphene follows Equation.2.4

$$E^{\pm}(k_x, k_y) = \pm\gamma_0\sqrt{1 + 4cos(\frac{\sqrt{3}k_x a}{2})cos(\frac{k_y a}{2}) + 4cos^2\frac{k_y a}{2}} \tag{2.4}$$

where γ_0 is the nearest neighbor hopping parameter, a is the lattice constant, k_x and k_y are the wave vectors in the Brillouin zone.

2.3.2 Carbon nanotube's crystal structure and electronic band structure

Based on the chirality, carbon nanotube can be divided into three types, namely armchair ($m = n$), zigzag ($m = 0$) and chiral CNT. This property can be uniquely characterized by a vector $\vec{C}$ in terms of two integers (n,m) corresponding to graphene vectors

$\vec{a_1}$ and $\vec{a_2}$[32] in Equation2.1(Fig.2.3(C)).
The carbon nanotube with chiral vector (n,m) can be defined as:

$$\vec{C} = n\vec{a_1} + m\vec{a_2} = (n, m) \tag{2.5}$$

And the circumference follows:

$$D = \frac{|D|}{\pi} = \frac{a\sqrt{(n^2 + nm + m^2)}}{\pi} \tag{2.6}$$

where a=$|a_1| = |a_2|$ is lattice constant of graphite around 2.4612 Å. The chiral angle θ of a CNT is given by Equation.2.7

$$\theta = tan^{-1}(\frac{\sqrt{3}m}{m + 2n}) \tag{2.7}$$

For energy dispersion relationship of CNT, we should make some modification to the relationship of graphene in Equation. 2.4. This modification comes from quantization of the walled wave vectors around the tube circumference restriction[33]. In the direction parallel to the CNT axis, electrons are free to move with larger distance, the electron wavenumber in the parallel direction $k_\parallel$ is effectively continuous. While quantized $k_\perp$ are determined by the boundary condition in Equation.2.8

$$\pi D k_\perp = 2\pi j \tag{2.8}$$

where j is an integer and D is the nanotube diameter. Inserting this boundary condition to Equation.2.4,the energy dispersion relation of carbon nanotube follows as.2.9

$$E_q^{\pm}(k_y) = \pm\gamma_0\sqrt{1 + 4cos(\frac{\pi q}{n})cos(\frac{k_y a}{2}) + 4cos^2\frac{k_y a}{2}} \tag{2.9}$$

Let k_y be along the Γ K direction, at the zone boundary $k_y = \frac{\pi}{a}$, the energy gap becomes $E = \pm\gamma$ (unlike graphene zero energy gap). The carbon nanotube's electronic conductivity depends on its chirality. When $n - m = 3q$, where q is an integral, the carbon nanotube is metallic, otherwise it is semiconducting. For approximation, for unseparated carbon nanotube, around $\frac{1}{3}$ of SWCNTs are metallic and the other $\frac{2}{3}$ SWCNTs are semiconducting.

Decompose the wavevector $\vec{k}$ into a component along the tube axis ($k_\parallel$) and a perpendicular vector as ($k_\perp$), and the band structure of carbon nanotube can be approximated by the Equation.2.10

$$E(\vec{k}) = \pm\frac{2\hbar v_F}{d}\sqrt{(\frac{m - n}{3} + p)^2 + (\frac{k_\parallel d}{2})^2} \tag{2.10}$$

Where, $v_F$is the fermi velocity and p is an internal, and $v_F = \sqrt{3}/2\hbar = 8 \times 10^5 m/s$ at $\gamma_0 = 2.9eV$. For a metallic nanotube, the dispersion relation near the fermi level satisfies Eq.2.11:

$$E^{\pm}(\delta\vec{k}) = \pm\frac{\sqrt{3}a}{2} \times \gamma_0|\delta\vec{k}| \tag{2.11}$$

For semiconducting tubes, this relationship becomes

$$E^{\pm}(k_{\parallel}) = \frac{\sqrt{3}a}{2}\gamma_0\sqrt{(\frac{2\pi}{|\vec{C_h}|})^2 \times (q \pm \frac{1}{3})^2 + k_{\parallel}^2} \tag{2.12}$$

Further simplify Equation.2.12 we can get the band gap of Equation.2.13

$$E_g = \frac{2d_{cc}\gamma}{\sqrt{3}d} \tag{2.13}$$

Considering γ is the nearest neighbor hopping parameter varies from 2.5-3.2 eV, from which follows that the band gap of a 1nm wide semiconducting tube is roughly 0.7 eV to 0.9 eV[34].

2.3.3 Mechanical properties of Carbon nanotubes

From an analysis of energy stability, a SWNT should be at least 0.4nm to afford strain energy in diameter and at most about 3.0 nm to maintain tubular structure[35–37]. Some distinguished physical properties of CNT comparing its allotropes (diamond, graphite, fullerene[38],graphene[39]) are listed in the Table.2.1 (After Ma et al[29].)

Table 2.1: Physical properties of different carbon material

Properties	Graphite	Fullerene	SWCNT	MWCNT
Density (g/cm^3)	1.9-2.3	1.7	0.8	1.8
Electrical conductivity (S/cm)	4000^p, 3.3^c	10^{-5}	10^2-10^6	$10^3 - 10^5$
Electron mobility $cm^2/(Vs)$	2×10^4	0.5-6	10^5	$10^4 - 10^5$
Thermal conductivity (W/(mK))	$298^p, 2.2^c$	0.4	6000	2000
Young's modulus (GPa)	350	NAN	1054	1200

where p means in-plane and c means axis.

Chapter 3

Gold nanoparticles

Gold, a nobel metal, has been used for aesthetic and curative purposes since ancient times. One of the most famous soluble gold works could be the Lycurgus Cup that was manufactured in 5th to 4th century B.C, which shows ruby red in transmitted light, and green in reflected light (Fig.3.2(B)). Nowadays, AuNPs are widely studied as chemical catalyst, self assembly monolayers (SAMs) components as well as molecular sensors in nanoscience[40]. Because of its unique optical, electronic and molecular recognition properties, AuNPs are widely believed to be a promising candidate for "point of care" molecular sensor [40–44].

3.1 Gold particles synthesis and assembly

In general, AuNPs for research purposes are prepared by two main methods, the Turkevich [45] and Brust-Schiffrin methods[46]. The Turkevich method involves the reduction of aqueous tetrachloroaurate (III) with sodium citrate, where citrate acts as a reducing and stabilizing agent that prevent growth and aggregation of nanoparticles (Figure.7.1 (B)[47]). While the Brust-Schiffrin method use a reaction of chlorauric acid solution with tetraoctylammonium bromide (TOAB) solution in toluene and sodium borohydride(Figure.7.1 (C))[48].

Freshly prepared AuNPs have an unstable core shell structure, which easily forms agglomeration under the change of concentration, pH or temperature. To prevent this phenomena, polymers (like Mercaptocarboxylic acid) with thiol group (forms gold-sulfuric bond) are often used to stabilize AuNPs solutions(Fig.7.1(A))[49]. These thiol stabilized AuNPs could be further functionalized to adjust its spacer arm length (polyethylene glycol (PEG)), or "cross linker" functionalization (for example biotinylation)(Fig.7.1(D)).

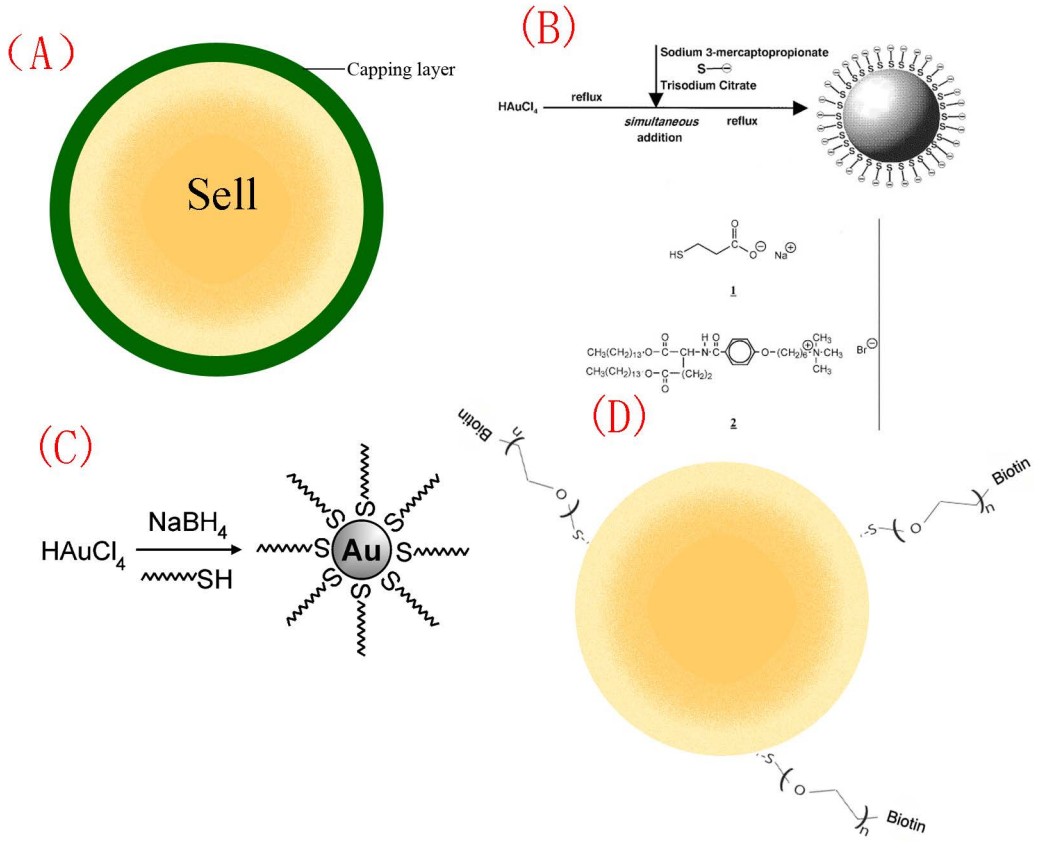

Figure 3.1: (A),Structure of gold particle, yellow part is the core shell of the gold particle, and green in the outer side is organic capping layer; (B) Preparation procedure of anionic mercapto-ligand stabilized AuNPs in water, from Ref[47]; (C) Formation of AuNPs coated with organic shells by reduction of Au^{III} compounds in the presence of thiols, from Ref[48]; (D) structure of biotinylated nanogold particle (5nm in diameter) used in the following experiment with average three binding biotin molecular

3.2 Optical properties of gold particles

From quantum mechanics, it shows that the electrons movement will be quantized if they are confined into very small objects. Gold particles can be thought as one of these objects, with diameter ranges from 5nm to 400nm. When the AuNPs's diameter is under 10 nanometer (thought of as "quantum dots"), size confinement effect will make gold particles to exhibit some unique optical and electrical properties[50]. In biophysics, researchers use these properties for detection of biomolecules, for example with surface plasmon resonance, or surface Raman scattering[12, 51].

Surface plasmon resonance (SPR) was first noticed by R.M.Wood[52] (1868-1955) at John Hopkins University, where he did diffraction's experiments with polarized light on metal backed glass. After that Gustav Mie[53]Lord Rayleigh[54], Palmer[55] have

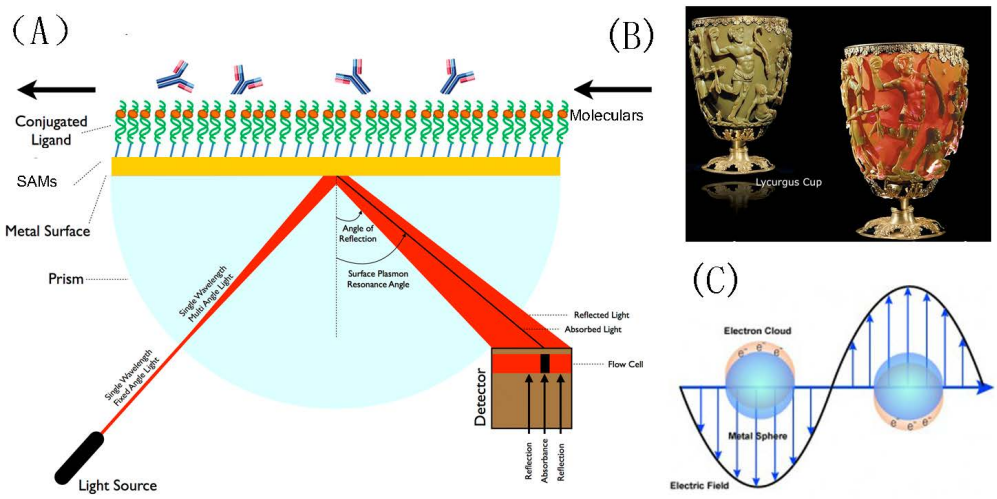

Figure 3.2: (A)Schematic of surface plasmon resonance detector, modified from wikipedia's surface plasmon resonance configuration; (B)Lycurgus Cup from British Museum website[60]; (C)Electron delocalization, a surface plasmon is characterized as a surface charge density wave at a metal surface[61].

tried to explained this phenomena in theory. In 1960th, Kretchman[56] and Otto[57] demonstrated that the attenuated total reflection light was due to surface plasmons and built the modern SPR sensor's basic structure. Liedberg[58], first used SPR to finish immunoassay with human IgG detection in 1983(See Fig.3.2(A)). This design has been utilized for immunoassays, biochemical sensor for practical detection[59]. For nanoscale particles, since surface plasmon resonance is restricted in nanometer-size, it is also called localized surface plasmon resonance.

Chapter 4

Biosensor

"A biosensor is a self-contained integrated device that is capable of providing specific quantitative or semi-quantitative analytical information using a biological recognition element (biochemical receptor), which is retained in direct spatial contact with a transduction element"[62]. In reality, a biosensors is usually composed of the following five components (Fig.4.1): (a) bioreceptor, translates information from the biochemical domain into a chemical or physical output signal (b) transducer, converts chemical or physical signal into electrical signal, (c) amplifier, increases transducer's signal; (d)signal processor, analyzes obtained data; (e) recording and display, presents the analysis result to the patient.

Figure 4.1: Schematic diagram of the main components of a biosensor

4.1 Characteristic of a biosensor

Some crucial characteristic of a biosensor includes linearity, sensitivity, selectivity and short response time. Here selectivity means that sensor detects a certain analyte and does not react to admixtures or contaminants[1]. Linearity means the relationship between the concentration of analyte and signal should be proportional in a linear relationship. Sensitivity means the biosensor's ability to detect low concentration of analyte. Finally, response time means how much time is required to fulfill one analysis process. Some other consideration of biosensor includes signal stability, cost of manufacturing and recyclability of the device.

[1] `http://www.biosensoracademy.com/eng/readarticle.php?article_id=11`

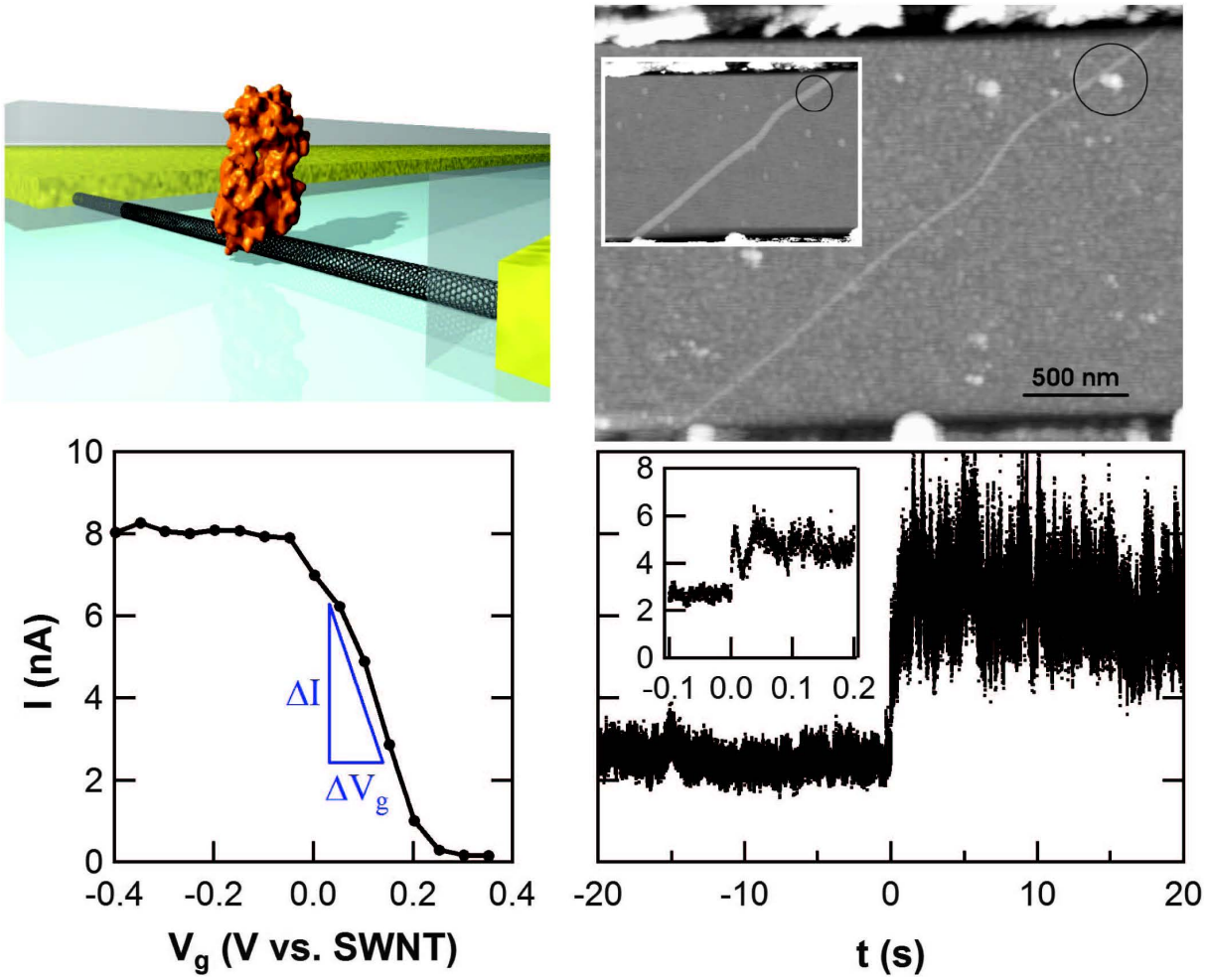

Figure 4.2: (A) Schematic diagram of the single lysozyme being interrogated by a carbon nanocircuit. The partial poly(methyl methacrylate) coating is depicted in gray. (B) AFM topography of a SWNT FET before (inset) and after coating with the pyrene linker, lysozyme incubation, and washing to reduce nonspecific binding. The circle highlights the point of lysozyme attachment. (C) Response of current in a lysozyme device to electrolytic gating. (D) I(t) measured in phosphate buffer, with peptidoglycan substrate (25 mg/ml) added to the solution at t = 0. The inset with a magnified time axis indicates a rapid response of less than 50 ms (inset) from Ref. [67]

4.2 Nanotechnology utilized in "point of care" biosensor

Immunoassay tests usually take place at large clinical labs which are far away from the patients' home. Sometimes, it takes too much time to give the feedback to patients that delays the entire recovery process. A new generation of fast and accurate "point-of-care" biosensor has been a hot research area in last decade [63–66]. Some promising results, for example interrogated single lysozyme on a carbon nanotube (Figure.4.2) has been made in 2012, and shows good response time and sensitivity.

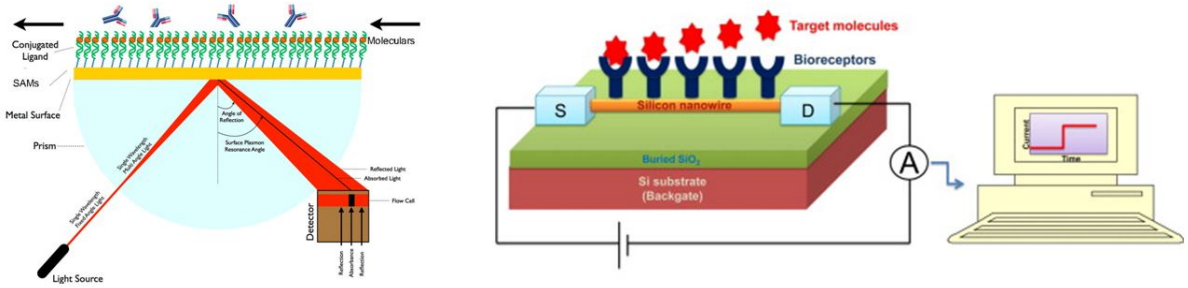

Figure 4.3: (A),Surface plasmon resonance detector from Wikipedia; (B), Field emission transistor of nanomaterial electronic circuit from Chen et al.[68]

Compared with traditional materials, two of the most obvious properties of nanoscale biosensors are: (a), a nanoscale biosensor has an extremely high surface to volume ratio which can interact directly with an individual biomolecule. In principle, a nanometer-scale biosensor is a device that could possiblly be used for detecting single proteins [67] (Fig.4.3(B), while in traditional biosensors the detection limit is one single layer (Fig.4.3(A)). (b), unlike intraditional biosensors, the nanomaterial usually is a part of the circuit, and this will further simplify the device and make it easy for home-use[12, 69, 70].

Chapter 5

Surface functionalization techniques

5.1 Physical and chemical adsorption

In an immunoassay or a biosensor test, the adsorption of biomolecules on a functionalized surface is usually the first step to think about. In practice, both physical and chemical adsorption approaches can be used. Physical methods include: (1) pure physical adsorption by hydrophobic or van der Waals forces; (2) Langmuir Blodgett method to compress one or more self-assembly layers on the surface; (3) microencapsulation to confine molecules into concave membranes (Fig.5.1(A)).

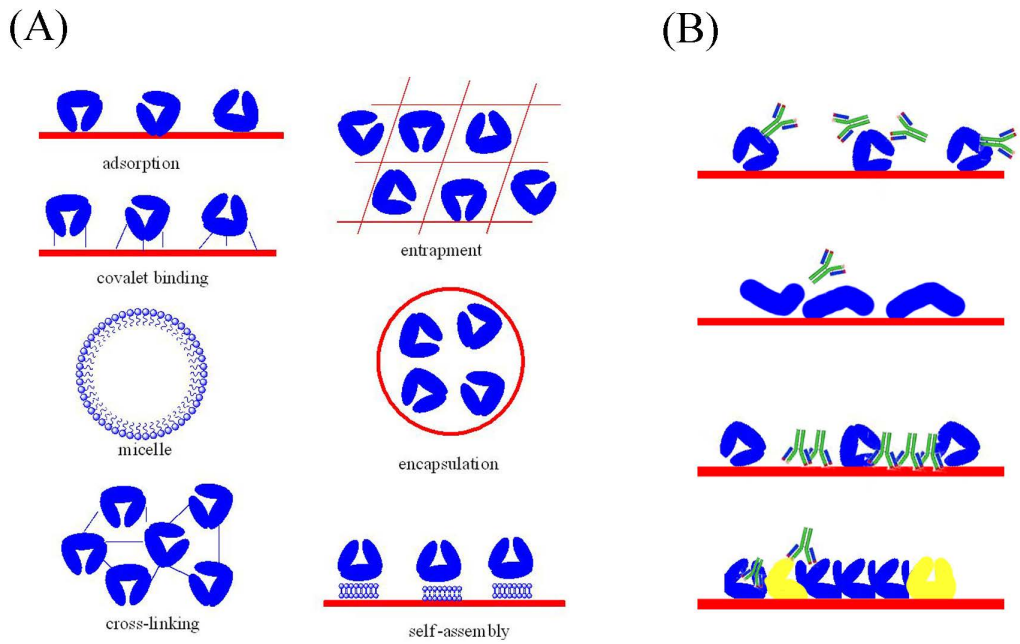

Figure 5.1: (A)Illustration of enzyme immobilization methods, from Wang et al [71]; (B)Difficulties in physical immobilization contains: loss of analyte binding capacity of immortalized protein; loss of signal transducing activity; nonspecific binding and lack of spatial specificity (from top to down).

Physical adsorption methods are usually easier to manipulate. However, it has inevitable drawbacks that makes it hard to predict molecular orientation. Without specific orientation, some unexpected results may lead to wrong conclusions (Fig.5.1(B)). For example: 1, Randomly oriented protein may hide its useful analytic binding group inside, which will result in signal loss; 2, Change of the protein's quaternary structure (common for membrane protein in Langmuir Blodgett method)during the immobilization process; 3, Nonspecific binding of analyte with surface that gives nonspecific signal from wrong places; 4, Lack of spatial specificity that limits a target molecule's function[12].

In practice, chemically functionalized surfaces with "cross linker" to control the orientation of biomolecule(see Fig.5.1(A)) are used in almost all experiments. Some critical parameters when selecting a proper crosslinker include target conjugation group, cleavability, water solubility and membrane permeability etc[1].

5.2 Silicon surface functionalization

Silicon is the most commonly used biosensor surface. It has a lot of distinguished properties in my mind, for example, (a), silicon has an atomically smooth surface that can give good contrast to small biomolecules (proteins are usually less than 10 nm in size) in topography; (b) modern microfabrication technology was mainly developed for silicon materials, there are mature experimental methods and equipments; (c), silicon can be easily oxidized to silicon dioxide and further reacted with silanes.

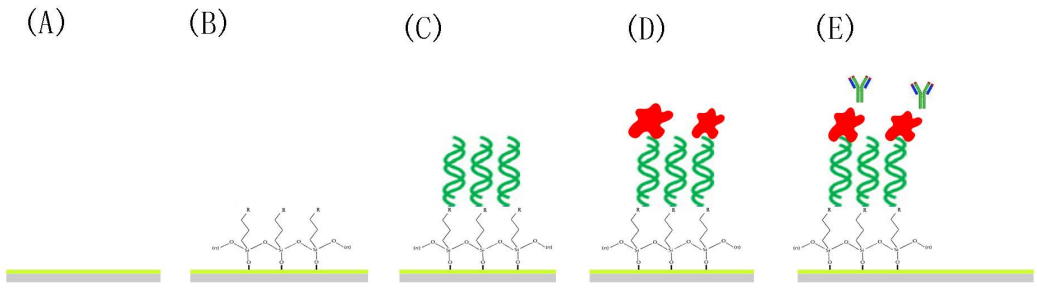

Figure 5.2: Schematic of preparing biosensor with silane; (A), cleaning the silicon surface and forms hydroxyl groups with piranha solution;(B) rinse the substrate with silane solution to form a self assembly functional layer; (C) add cross linker for immobilization of protein; (D) immobilization of research protein; (E) bind the analyte with researched protein for detection

[1] http://www.piercenet.com/browse.cfm?fldID=26436A16-60A0-4A56-85F7-213A50830440

The whole structure of functionalized silicon surface looks like a "sandwich"(Fig.5.2(E)), where the immobilized biomolecule's orientation and spacial density could be controlled by a cross linker. A classical method of silicon functionalization[12] includes five steps. In the first step, cleaning organic contaminants on the silicon surface and generate reactive hydroxyl (-OH) groups (Fig.5.2(A)) with piranha solution (mixed sulfuric acid and hydrogen peroxide) or reactive ion etching. In the next step, reactive hydroxyl group is substituted by silane solution and forms self-assembly monolayer(SAM)(Fig.5.2 (B)). After that, cross linker molecules for specific ligand (primary amine, amine, carboxyl, carbohydrate, hydroxyl, sulfhydryl, thymine, hydrazine etc[72]) on target molecules will be added(Fig.5.2(C)). In the final steps include target protein's incubation for immunoassay test (Fig.5.2(D)-(E)).

5.3 Carbon nanotube's surface functionalization

For state of art, the most common carbon nanotube based sensor is to assemble it in a field effect transistor(Figure.5.3). On which a set of carbon nanotubes is connected with source and drain terminals in the circuit, and gate terminal is used for controlling current. Some analytic device like chemical sensor (NO_2[73], NH_3[69] gas sensor), mass sensor[74],optical sensor[75], ion sensor[76]and biosensor[77, 78]etc have already been designed.

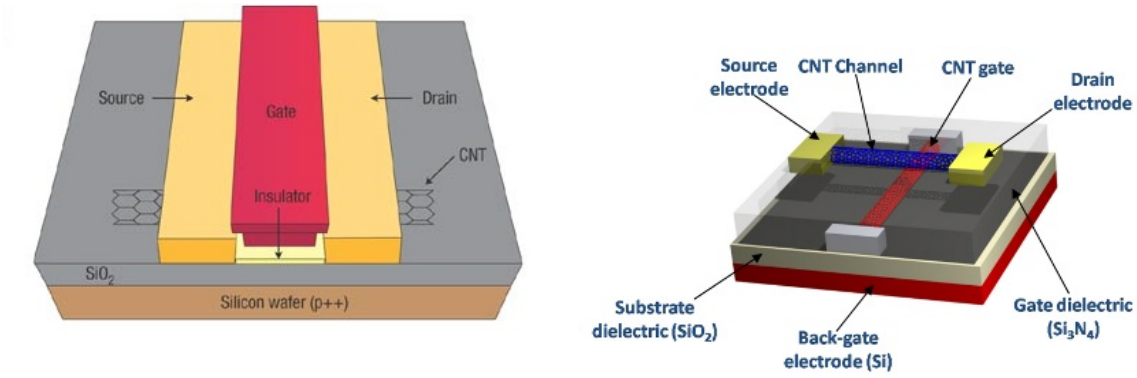

Figure 5.3: Left:Side view of a back gated carbon nanotube field effect transistor, from Avouris et al[79];Right: Side view of a suspended carbon nanotube based field effect transistor[80]

5.3.1 Covalent functionalization of carbon nanotube

Covalent functionalization of carbon nanotubes use active carbon atoms on CNTs as precursor for silanization, polymer grating, esterfication, thiolation, alkylation and

arylation processcite[29]. These active carbon atoms usually comes from the following two areas: (A)"Stone-Wales" defects, where six membered rings of graphene transfer into the mixture of pentagons and heptagons(see Fig.5.4(A)); (B), rehybridized carbon atoms at the capping areas on CNT[81]. From simulation and Raman spectrum, it predicts that these activated carbons typically accounts for 1-3 percents of al the atoms in pristine carbon nanotube[82].

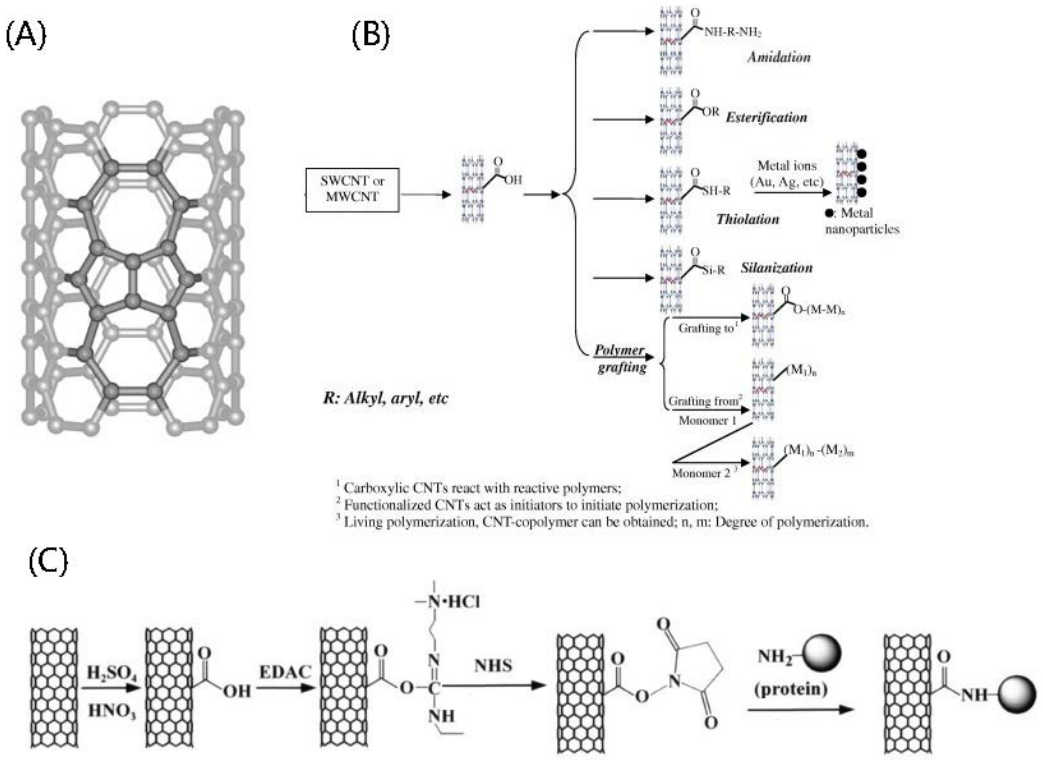

Figure 5.4: (A) Stone-Wales defect on the sidewall of nanotube. Kannan Balasubramanian and Marko Burghard[82]; (B) Strategies for covalent functionalization of CNTs (AL direct sidewall functionalization; B: defect fictionalization) Figure from Peng-Cheng Ma, Naveed A. Siddiqui et al[29].(C)Schematic view of the attachment of proteins to carbon nanotubes via a two-step of dimmide actived amidation. Modified from Jiang et al[83].

For covalent functionalization of carbon nanotube on CNT's sidewall, some common methods include: oxidize to hydroxyl group (-OH) or carboxyl group (-COOH), fluoride to carbon-fluoride bond (C-F)[84], halogenate CNT to C-Cl or C-Br bonds[85] etc. Focusing on CNT's oxidization(see Fig.5.4(B)), common oxidants like piranha solution[86], $KMnO_4$[87], ozone[88, 89] and reactive plasma[90] have already been used. A routine analyze process often included scanning electron microscopy images and infrared spectrum (or Raman spectrum) before and after oxidation. However, this method does not provide any information about CNT's mechanical or electrical property variation. It is equally possible that, the CNT's integrity has already been

broken during the functionalization process, which turns to be useless when they are assembled into the electronic circuit.

After oxidation, the next step for molecular binding modification was adding cross linker. One of the so called "universal" methods for protein immobilization is the NHS-EDC method. This method uses a two-step process with N-ethyl- N' -(3-dimethylaminopropyl) carbodiimide hydrochloride (EDAC) and N-hydroxysuccinimide (NHS) to specific binding with protein's α amino groups[83](Fig.5.4(C)). The reaction mechanism in short can be explained as following: carboxylic acid groups on the carbon nanotube was first reacted with EDAC, forming a highly active O-acylisourea ester. This intermediate can form a more stable succinimidyl intermediate ester with NHS. The amine reactive NHS ester can function with the primary amine group on protein to finally form stable conjugate by amide bonding[2].

5.3.2 Non-covalent functionalization of carbon nanotube

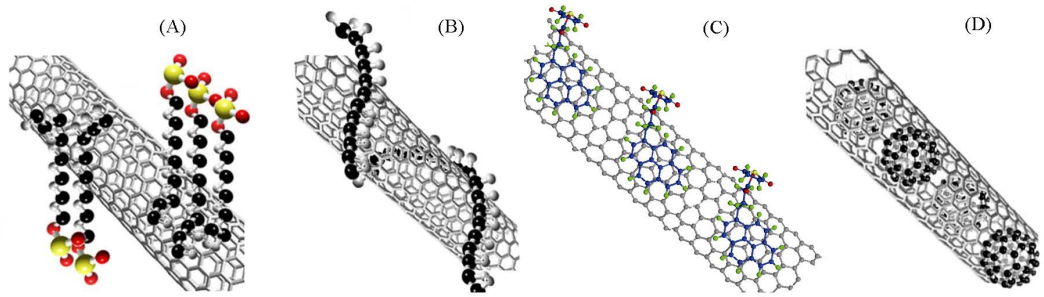

Figure 5.5: (A), Noncovalent adsorption of surfactant; (B), Wrapping of polymers; [91] (C) 1-pyrenebutanoic acid succinimidyl ester adsorption of carbon nanotube (modified Figure from Fan et al. [92]); (D) endohedral functionalization of C_{60}

Non-covalent functionalization or physical functionalization of carbon nanotubes does not depend on the active carbons or defects on the CNT's structure. So in principle, it will not destroy the conjugated system of the CNTs sidewalls[91]. From different functionalization principles, physical treatment on carbon nanotubes can be classified as polymer wrapping (Fig.5.5(B)[93–95]), surfactant adsorption [96, 96–98] and endohedral methods etc[29]. Some of the promising results for biomolecular detection with physical functionalization, for example, by 1-pyrenebutanoic acid succinimidyl ester was first used by Dai et al. This method can also be thought of as universal method for specific binding with protein's primary amino group[14, 15, 99](see Fig.5.5(C)). For short, 1-pyrenebutanoic acid succinimidyl ester adsorption on the sidewall of CNT by $\pi - \pi$ binding, and the succinimidyl ester will covalently bind with a primary amine

[2] `http://www.piercenet.com/browse.cfm?fldID=02040114`

group on a protein.

5.3.3 Comparing physical and chemical functionalization of CNTs

Physical and chemical functionalization methods in CNTs have already been widely researched during the last decade with numerous outstanding experiments and computer simulations. In general, these two methods have their own advantages and disadvantages which usually come from the methods itself and can not be eliminated.

Table 5.1: Advantages and disadvantages of various CNT functionalization methods

Method		Principle	Damage	use	Interaction
Chemical Method		Sidewall Hybridization sp^2 to sp^3	Yes	Easy	Strong
Physical Method	Polymer wrapping	Van der Waals force, π-π stacking	No	Easy	Variable
	Surfactant adsorption	Physical adsorption	No	Easy	Weak
	Endohedral	Capillary effect	No	Hard	Weak

Part II

Experiment and Discussion

During this one year master experiments, several characterizing tests with proteins, gold particles, carbon nanotubes and limited biosensor work have been finished in Nanoscience center in Jyvaskyla. In order to show these experiment in a more logical way, I list the experiment as following:

1. Imaging surfaces and nanotubes

   (a) AFM studies of atomically smooth surfaces (mica, highly ordered pyrolytic graphite, silicon etc)

   (b) Fabrication with e-beam lithography of markers on graphite

   (c) Single-walled carbon nanotube and multi-walled carbon nanotube deposition and imaging with AFM

   In the first part, I will show the experiments on AFM imaging of surfaces including graphite, silicon, mica, and also of carbon nanotubes. Some additional experiments include: (A), how to fabricate AFM markers on graphite in Section.6.3; (B), different methods of oxidation on graphite surface in Section.6.2

2. Imaging isolated proteins and gold nanoparticles

   (a) Chimeric avidin deposition and imaging with AFM

   (b) Biotinylated gold particles deposition and characterization with AFM and scanning electron microscope

   In the second part of experiment, I focus on detection of isolated compo- nents of future biosensors. AFM and SEM imaging target molecules - chimeric avidin and analyte - and biotinylated gold particles are tested. An interesting "extra" result was found in self-assembly of mono- layers of gold particles. This work was mainly done with the help of bachelor student Hannu Pasanen, for details see Section.7.2.

3. Functionalization of nanotubes with protein

   (a) Covalent and noncovalent binding of chimeric avidin and carbon nanotube with AFM and detection with SEM

   In the last part, I will show a simple functionalized carbon nanotube structure with protein immobilization. Definitely, this is not the end of biosensor research at this stage, much more testing will follow.

Chapter 6

Imaging surfaces and nanotubes

6.1 Fresh mica and graphite surface

Muscovite mica ($KAl_2(Si_3Al)O_{10}(OH)_2$) and highly ordered pyrolytic graphite (HOPG) have highly ordered crystal structures. Under force along cleavage planes, these two material can form atomic-level smooth fresh surfaces for biological purposes (Fig.6.1(A)-(C)). On fresh HOPG's surface, it is mainly composed of non-polar carbon-carbon bonds, which makes graphite with obvious hydrophobic property(Fig.6.2(A)). While, muscovite mica is a mineral, which has large amount of covalent bonds and is in general much more preferable to affinity of water molecules.

In this experiment, the fresh mica material and graphite was first fixed on the aluminium plate with double side tape. After that, I carefully removed off some top layers of the materials by 3M "scotch tape". These freshly cleaved graphite and mica were then quickly transferred into a scanning force microscope to analyze the smoothness of the surface and height variation of the cleavage steps. From Fig6.1.(D) and (G), it clearly shows that in micrometer scale, both graphite and mica can be considered as smooth on sub-nanometer scale. Mica surface has much less linear dislocations density (cleavage steps) than graphite surface using scotch tape method. Considering most large biomolecules, like DNA or protein's height variation usually in nanometer scale, these two surfaces are both suitable for their detection.

6.2 Hydrophilic treatment of graphite

Hydrophilic treatment of graphite in this thesis means forming graphitic oxide (a compound of carbon, oxygen and hydrogen in variable ratios), like epoxy bridges, hydroxyl groups or carboxyl groups on the graphite surface. Depending on whether using liquid solution, hydrophilic treatment can be classified into dry hydrophilic treatment and wet hydrophilic treatment. In this research, I chose reactive oxygen plasma as dry

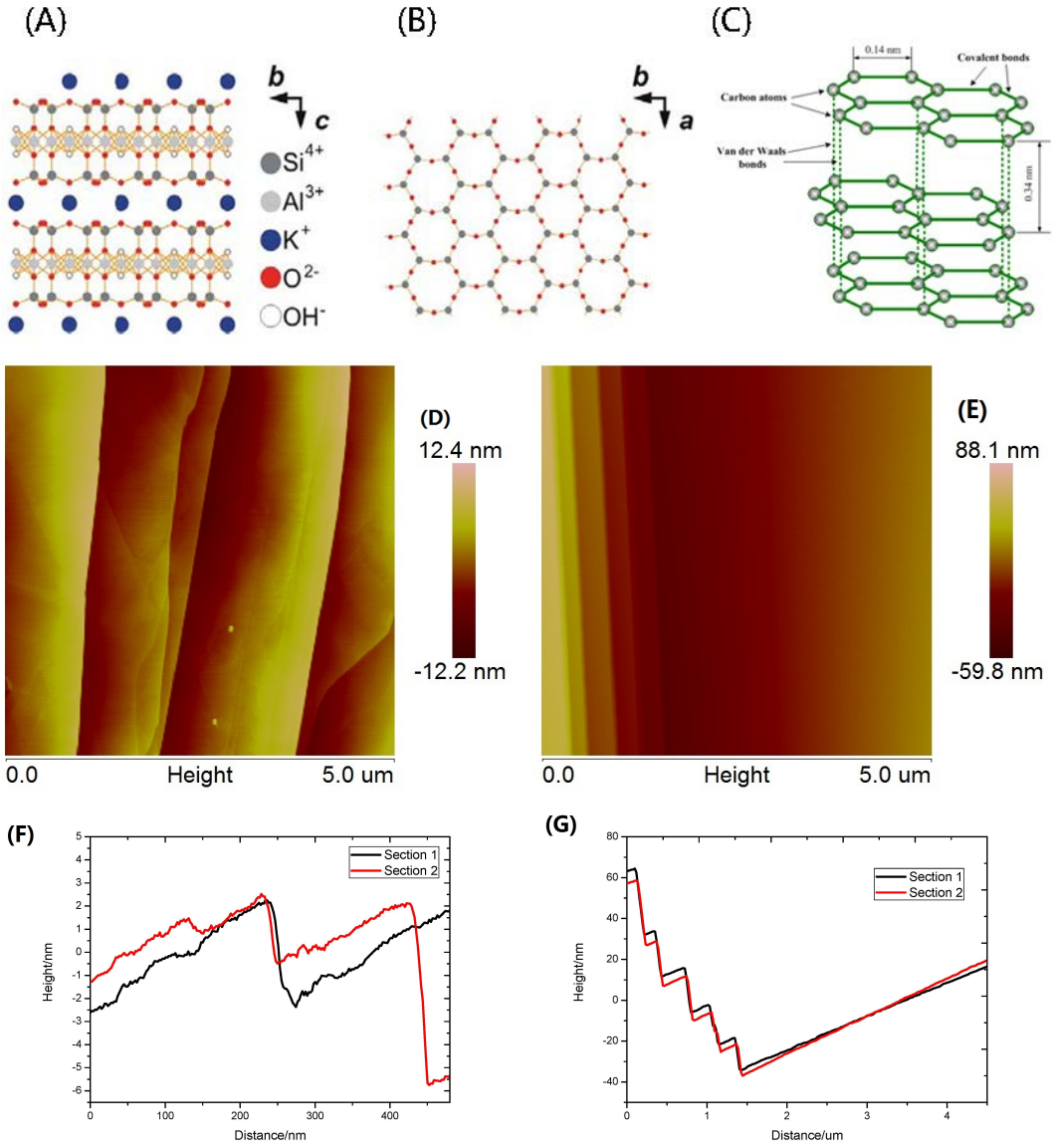

Figure 6.1: Top: Schematic representation of the muscovite mica crystal structure. Vectors a and b define the 001 planes, vector c is the surface normal vector.(A), Side view (projection onto the a-axis) exhibiting aluminosilicate layers separated by electrostatically bound interlayer potassium inons. (B), Hexagonal arrangement of the 001 surface top layer (projection onto the c-axis) exhibiting Si(Partly Al) and O atoms of a cleaved mica surface, residual potassium ions are not displayed. Reprint from Ostendorf et al [100](C), Crystalline structure of graphite, σ-σ bonding in the Basal plane is 0.14 nm, Van der Waals and π-π bonding between each Basal planes is 0.34 nm. (D), Height image of fresh graphite surface; (E), Height image of fresh mica surface, scanning sizes of 5 micrometers; (F), Section height data of graphite surface; (G), Section height data of mica surface

hydrophilic treatment, hydrogen peroxide, mixed acid (concentrated sulfuric acid and nitric acid) for wet hydrophilic treatment.

Fresh $5mm \times 5mm$graphite chips were dipped in mixed acid (1:3 volume ratio of condensed sulfuric acid and nitric acid) or 4% hydrogen peroxide solution (kept at 4 Celsius) for variable times. After incubation, these chips were transferred to a homemade contact angle goniometer to record their contact angle by adding 20 microliter millipore water. The contact angle of a static water drop reflects the properties' changes on the surface. Some explanation for this phenomena is as follows. As it is known, that the water molecule is a polar molecule with positive dipole δ^+ near hydrogen atoms, and δ^- at oxygen atom. Compared with binding with non-polar groups, it can form weak electrostatic attraction to polar bonds (like carboxyl group, hydroxyl group etc), which are produced in hydrophilic treatment. Therefore, the drop contact angle of the droplet should be smaller if there are more polar groups on the graphite surface. The results of hydrogen peroxide treatments are shown in Fig.6.2(1-7), and the droplets' edge detection with Mathematica are shown in Fig.6.2(A-G).

Dry hydrophilic treatment with reactive ion oxygen gas has similar reaction mechanism with wet etching. Oxygen gas is ionized into oxygen ions and electrons under high electronic voltage. When these oxygen ions hit a graphite surface, they can break carbon-carbon bonding and form carboxyl groups on the sidewall of the CNT. The recipes used for dry hydrophilic treatment were: Oxygen 50 sccm, temperature 30 $^\circ C$, power 300W, radio frequency 13.56 MHz, and reaction times varies from 10 second to 10 mins. Their reaction results are shown in Fig.6.2(2-4 or B-D).

Comparing the contact angle of pure water on fresh graphite surface (Fig.6.2(1)) to hydrophilic treatment results(Fig.6.2(2-7)), it shows clearly decrease of the contact angle. Furthermore, we can see that hydrogen peroxide treatment (Fig.6.2(5-6)) and reactive ion etching methods(Fig.6.2(2-4) have similar hydrophilic ability of graphite, which does not totally break sp^2 bonding between each Basal planes. Here, 3 hours of mixed acid treatment has the strongest effect on graphite structure. After this treatment, the graphite sample broke into three pieces, whereby no water droplet can stand on its surface. Carefully check with optical microscope shows that there are obvious cracks on the surface, which could possible be produced by the heat in the reaction. One possible use of this mix acid method is to break π-π bonding between Basal planes. Hydrophilic treatment's results varies with treatment time, and logically we expect that longer etching causes more functionalization groups and therefore more hydrophilic property of graphite surface. For further research, this is a complicated issue, which will not be fully discussed at this stage.

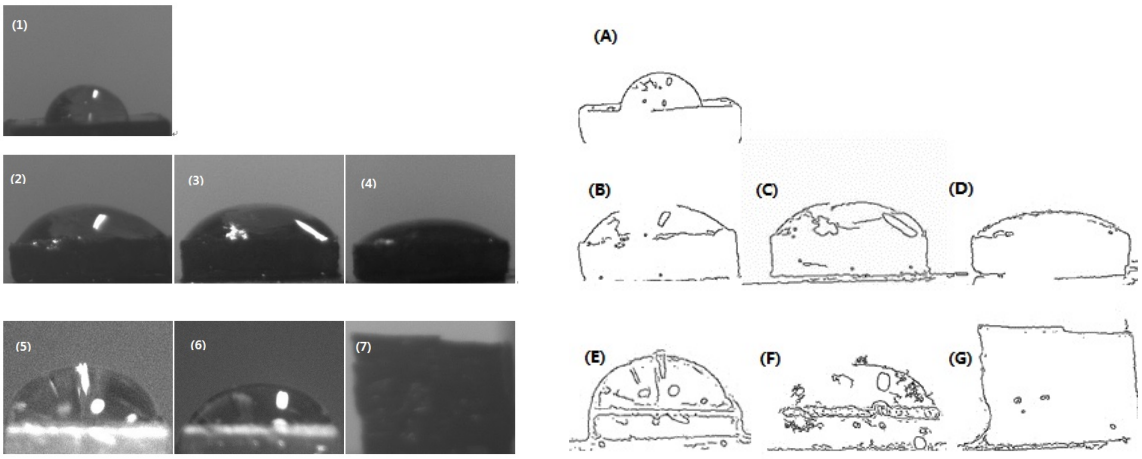

Figure 6.2: (1)Contact angle of millipore water on fresh cleavage graphite; (2)10 second reactive ion etching hydrophillic treatment; (3)1 min reactive ion etching hydrophillic treatment; (4)10 mins reactive ion etching hydrophillic treatment; (5) 15 mins hydrogen peroxide treatment; (6) 1 hour hydrogen peroxide treatment; (7) 3 hours mixed acid treatment;(A)-(G) Edge detection of droplets with different hydrophilic treatment on graphite

6.3 Scanning force microscope's markers on graphite

The Scanning force microscope (mainly the AFM) is very limited with respect to scanning area and scanning speed. By necessity, prefabricated AFM markers, with around 10 μm separation, are widely used to locate scanning areas for nanometer scale objective detection. For substrates of graphite, traditional microfabrication process for microelectromechanical systems(resist spin- ning, lithography, development, metallization, lift-off) does not work so well. The limit mainly comes from the graphite's cleavage properties under lateral force and the possibility of chemical residues. To overcome these drawbacks, I tried to only use silicon nitride mask and metallization to manufacture gold markers on graphite surfaces.

6.3.1 Mask wafer preparation

12 cm diameter silicon nitride wafer with 550 μm thick silicon with 300 nm silicon nitride layers on each side was first cut into 80mm $\times$ 80mm squares wafers with LOADPOINT MicroAce 3 dicing saw. It was cleaned by deionized water and normal microfabrication cleaning process (acetone and isopropanol (IPA)) to remove organic material on the surface. After nitrogen gas gun drying, double layers of commercial ebeam lithography resist(PMMA A7%) was spinned on both topside and backside of raw substrates with spinning speed 3000rpm for 1 minute. Here, the backside of PMMA was optional, and it was used as a protection layer during the first silicon nitride etch-

ing process. Sample baking were done on hot plate (160 $^{\circ}C$) of 2 mins to evaporate solvent and smooth the resist after each spinning period.

6.3.2 Backside ebeam lithography

Based on mask area design purpose, a 1200 μm $\times$ 1200 μm square window was first fabricated on the backside. This process can be done either with ebeam lithography or photolithography. In this experiment, I used Raith E-line electron beam lithography in this process. After exposure, the sample was dipped in 1:3 of MIBK (methylisobutylketone): IPA (isopropanol) of 45 seconds for development.

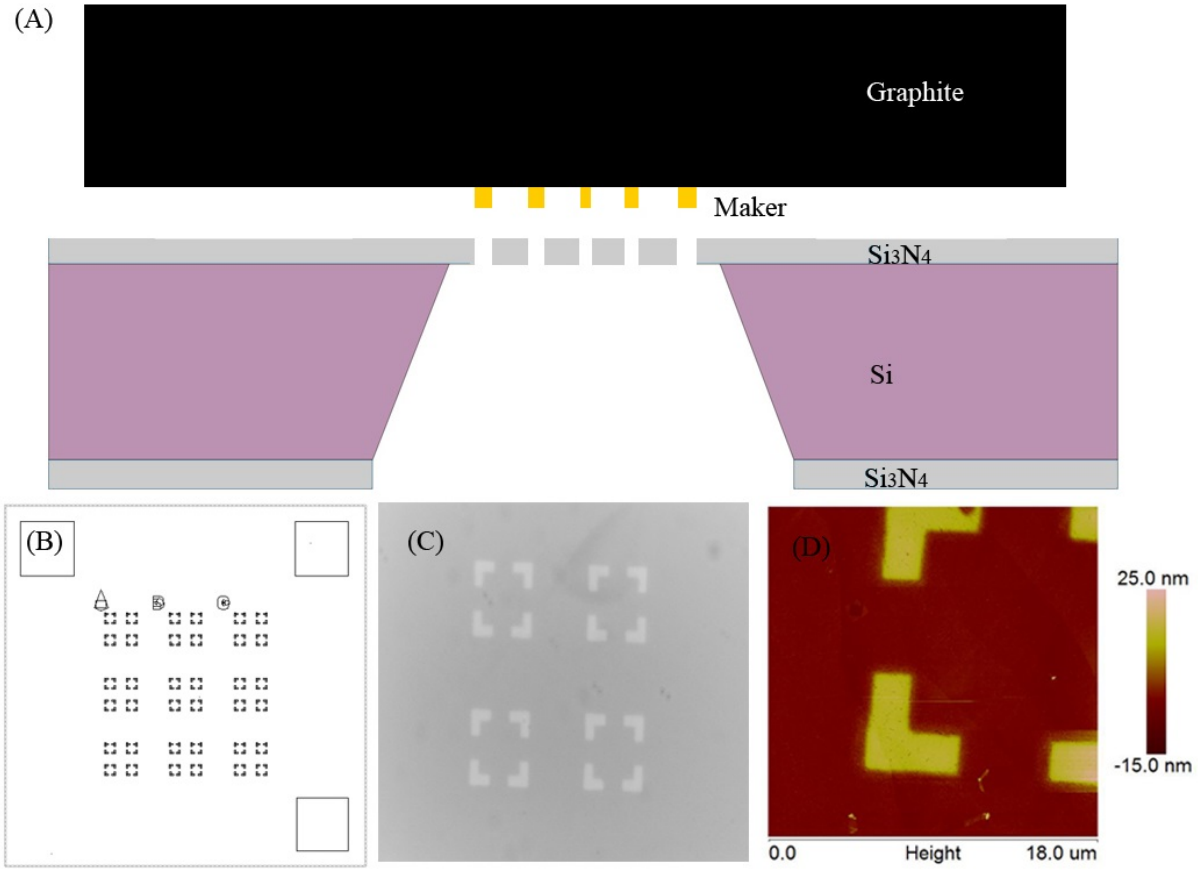

Figure 6.3: (A)Schematic of graphite mask structure; (B)Topside electron lithography CAD pattern; (C) Optical microscope image of gold markers on graphite (greyscale); (D) AFM height image of markers on the graphite, with scanning size of 18 micrometer, and height bar from -15nm to 25nm. AFM image from Kosti Tapio.

6.3.3 RIE etching of Si_3N_4

The backside silicon nitride not covered by protection PMMA was then etched away in Oxford Instruments Plasmalab80 Plus reactive ion etching. The recipe used for Si_3N_4 etching were: Trifluoromethace (CHF_3) 50sccm and oxygen(O_2) 5 sccm under 30 $°C$and pressure of 55 mTorr of 15 mins. From previous experiments, we know the etching rate in z direction should be 26nm/min with this recipe. After RIE etching, the window was carefully checked under optical microscope, and it should look like a white color square on pink silicon nitride substrate depending on the thickness of silicon nitride.

6.3.4 KOH anisotropic etching of Si

The substrate with opening window on topside was then transferred to KOH etching bench. Here, 35% KOH (potassium hydroxide) was used as etching reactant at 98 $°C$for 5 hours. This wet etching process is an anisotropic process along the silicon (100) plane. After KOH etching, the chip had to be carefully washed four times in hot water to to take off residual KOH. The etching angle of anisotropic silicon is 54.7 ° following Si's (100) crystallographic planes, forming pyramidal cavities[101, 102]. The relationship between topside silicon nitride window's area and the silicon nitride membrane on backside follows Equation.6.1

$$l = L - \frac{2d}{tan54.7} = 490\mu m \tag{6.1}$$

where L is the length of square in the backside, d is the thickness of the silicon of the chip, and l will be the side length of the window in the topside. Since the window on the backside is $1200\mu m \times 1200\mu m$, after KOH etching a $490\mu m \times 490\mu m$ membrane could be manufactured. Further fine ebeam lithography (AFM pattern lithography) was confined on this topside membrane.

6.3.5 Fine structure ebeam lithography on topside

Repeated sample preparation process as Section6.3.1 was done for the topside silicon nitride membrane. The fine structure patterning on topside is designed as Fig.6.3(B), where the area of one scanning square is $10\mu m \times 10\mu m$. This distance was a good compromise between AFM scanning speed and tip location accuracy. After ebeam lithography, repeated development, and silicon nitride plasma etching process was done as in Section.6.3.3.

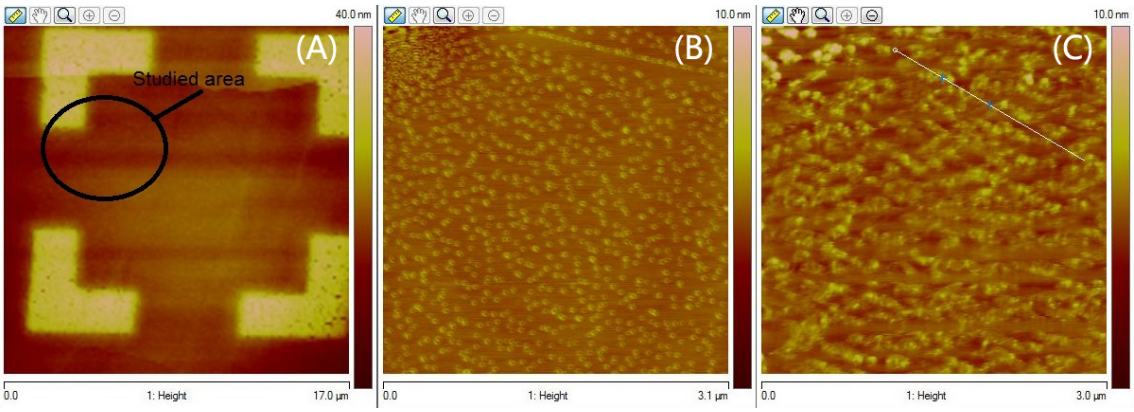

Figure 6.4: (A), Graphite marker before treatment, black circle define the location of target research area; (B), target area before treatment; (C), target area after avidin treatment

6.3.6 Metallization

The graphite mask with graphite sample was assembled (as Fig.6.3(A)) and put into physical evaporator for metallization. Under ultrahigh vacuum (10^{-8}mbar), a total thickness of 15 nm thickness gold was evaporated on the graphite surface with evaporation speed of 1 Å/s. No lift-off or cleaning process was needed after metallization. From optical microscope (Fig.6.3(C))and AFM (Fig.6.3(D)) images, the gold patterning on graphite is sharp and space between neighboring fine marker is clean, which is crucial for the next immobilization process.

6.3.7 Usage of graphite mask

Graphite mask can be used for a lot of biomolecule detection research. M.Sc.Kosti Tapio from the Nanoscience Center used this mask on graphite for avidin height detection (Figure.6.4) in the same area.

6.4 Adsorption carbon nanotube on silicon

Single walled carbon nanotube from Karlsruhe Institute of Technology[1] and multi-walled carbon nanotube (O.D.$\times$ L 7-12 nm $\times$ 0.5-10 μm) from Sigma-Aldrich company[2] were first dissolved in the 1,2-dichloroethane(Fig.6.4(B)) with sonicator. Before each deposition, the CNT solution has to be sonicated for 25 minutes again to dissolve the bundles(Fig.6.4(B)). I dipped carbon nanotubes solution on IPA-washed silicon surface at 3000 rpms for 60 seconds.

[1] `http://www.kit.edu/english/`
[2] `http://www.sigmaaldrich.com/catalog/product/aldrich/406074?lang=fi&region=FI`

Figure 6.5: (A)FinnSonic sonicator used in the experiment; (B)Dispersed single walled carbon nanotubes in 1,2-dichloroethane

From AFM images of Fig.6.6, it shows that the diameter of Aldrich multiwalled carbon nanotube on the silicon is around 6nm (Fig.6.6(A and C)), while the diameter of Karlsruhe single-walled carbon nanotube is 2.5nm (Fig.6.6(B and D)). The intensity of carbon nanotube on the surface was low enough to distinguish single CNT and no significant bundles of carbon nanotubes was found. This proved the suitability of 1,2-dichloroethane to dissolve carbon nanotube bundles.

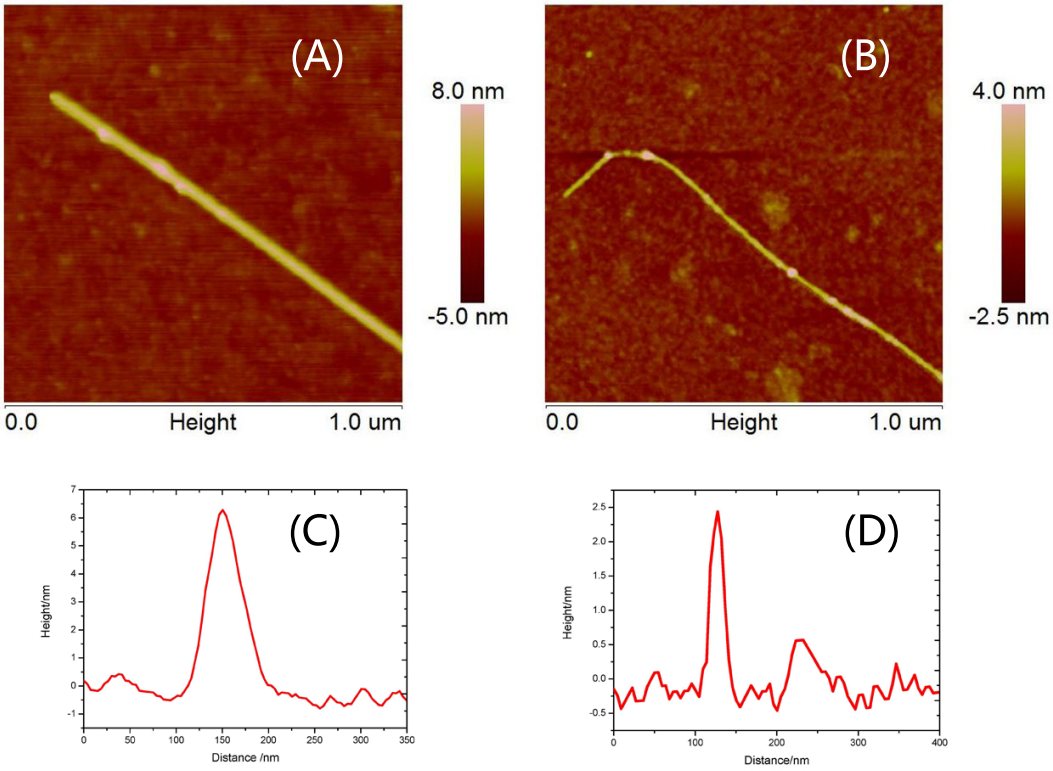

Figure 6.6: (A)Height image of multi-walled carbon nanotube; (B) height image of single-walled carbon nanotube, with scale size of 1 micrometer; (C) and (D) scanning section data of multi-walled carbon nanotube and single-walled carbon nanotube

Chapter 7

Imaging isolated proteins and gold nanoparticles

7.1 Biotinylated gold particle on silicon

In this experiment, biotinylated gold particle with diameter of 5 nm was used as a detector for avidin-like proteins. So it is crucially important to detect a single gold particles on the surface. Usually in this size of AuNPs, transmission electron microscopy was a better choice for its higher resolution. However, for TEM, its standard $\phi 3$ chip made of copper limits a lot for the next step in the assembly. So in this experiment, only scanning force microscope and scanning electron microscope were used. In this experiment, evaporation method was used for self-assembly of monolayers, spinning method was adopted for single AuNPs location and detection.

To find identical biotinylated gold particles with diameter of only 5nm on the surface of silicon, it needs extremely small error tolerance that needs AFM markers (Fig.7.1(A)). The AFM maker used in this for biotinylated AuNPs is designed as in Fig.7.1, and the distance between neighboring cross fine structures is 7 micrometer.

After hydrophilic treatment of the silicon surface (2 mins oxygen surface cleaning in RIE), 4.5×10^{-6}mol/L biotinylated gold particle solution was spined on it with 1000 rmp. During the spinning period, a majority of AuNPs spinned away, and only very small amount of AuNPs stayed. Compared with AFM image (Fig.7.1(A)) and SEM image (Fig.7.1(B)) in the same place, it clearly showed that Raith Eline equipped with "in-lens" detector can be used for detection of around 5 nm sized AuNPs.

One of the most challenging work with 5 nanometer AuNPs is their such small interaction volume (Figure.7.1 (A)). As we know, the working mechanism of scanning electron microscope's detector is to amplify a weak signal into a photon flux under several times photoelectron transforms through a photomultiplier tube. These signal

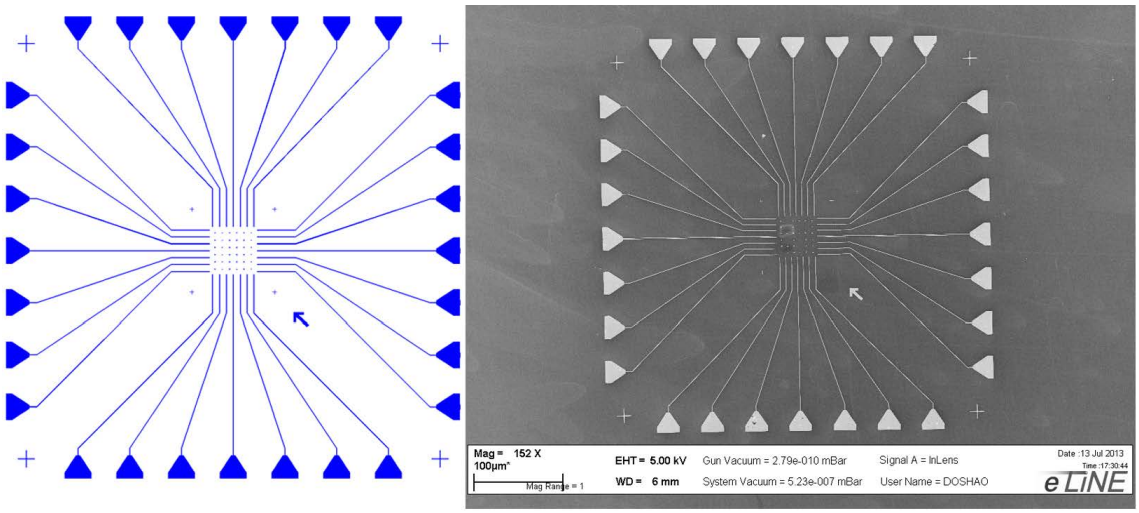

Figure 7.1: (A), CAD design of AFM markers for biotinylated gold partcles; (B) SEM images of AFM markers on silicon

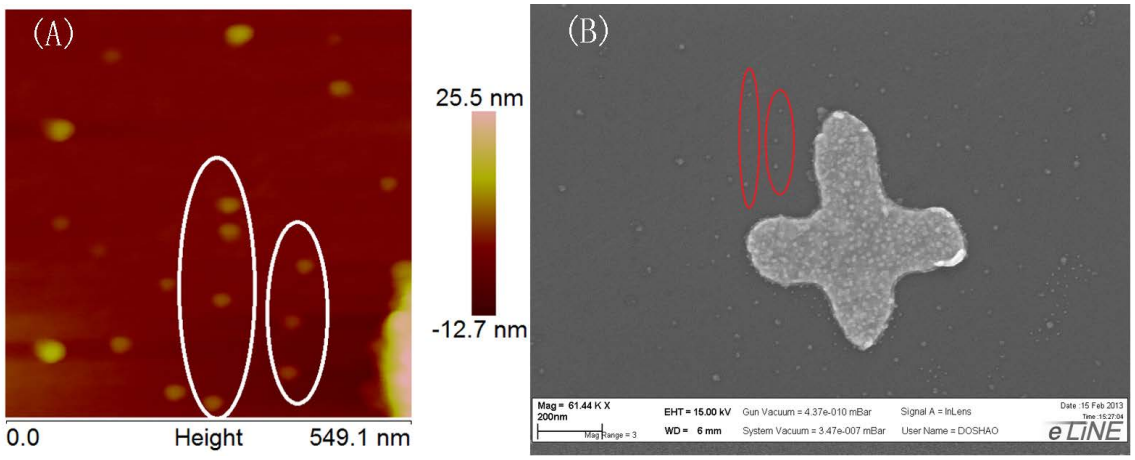

Figure 7.2: (A)aptitude image of AuNPs on the silicon; (C) SEM image of AuNPs on the silicon in the same place

mainly come from two resources, backscattering electrons (elastic interactions of nuclei of atoms) and secondary electrons (ejected valence electrons). The intensity signal of both backscattering electrons and secondary electrons are proportional to sample's volume, so in this cases, it is very hard to detection such small gold particles.
In order to explain how signal changes with gold particle's diameter variation, I made one Monte Carlo Simulation (Figure.7.1 (C)-(E)). This electron trajectory simulation is based on the following model: $10nm \times 10nm \times 50nm$ pure silicon with 2 nm native silicon oxide was first set up as the substrate; on top of the silicon oxide, one gold particle (diameter of 5nm) without organic layer was placed in the middle. Based on the practical E-line parameter, the diameter of electron beam is 2 nm at electron voltage of 20 keV (Figure.7.1(C)). In total 2000 electron trajectories are simulated at the same time, and for transmitted electrons are labeled with blue color, the backscattering

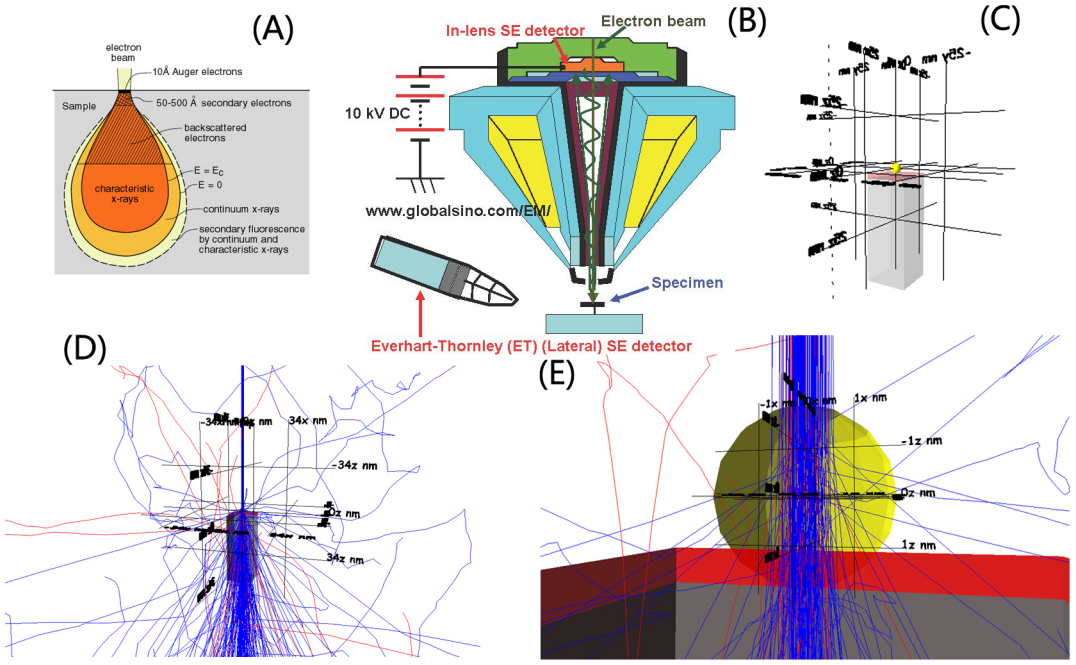

Figure 7.3: (A), Generalized illustration of interaction volumes for various electron specimen interaction. Auger electrons and secondary electrons comes from very thin region of the sample surface from 1nm to 50nm. Reprinted from James H.Wittke[103]; (B)Position of "in lens" detector and traditional Everhart Thornley detector in the sample chamber. Picture from Practical electron microscopy and database[104]; (C), Casino (Monte Carlo Simulation of electron trajectory in solids) model, with 5nm gold sphere (yellow), 2nm thickness native silicon oxide, and 50 nm thickness of silicon; (D) and (E) Simulation results of electron trajectories, red ones are backscattered electrons.

electrons are labeled with red ones (Figures. 7.1(D-E)). Besides that, from Figure.7.1 (E), we can also observe that most backscattering electron trajectories are nearly in the opposite direction of primary electrons. This conclusion may explain why "in-lens" detector is very useful in this experiment.

In Raith E-line there are three detects: one normal Everhart-Thornley secondary electron detector (Figure.7.1(B)) nearly horizontal direction of the specimen; one backscattered electron detector; and one InLens secondary electron detector (also the default use detector) vertical to the sample(Figure.7.1(B)). Energy-filtered "In-lens" detector was first built for high resolution low energy backscattered electron[105]. It is not a single electron detector, but a set of four electron detectors (Figure.7.4(B)). Among these four detectors: Annular BSE-detector and Annular SE-detector are called energy selective BE detectors (EsB detectors); the other two detectors, low angle BSE and high angle BSE detectors are called angular selective BE detectors (AsB detec-

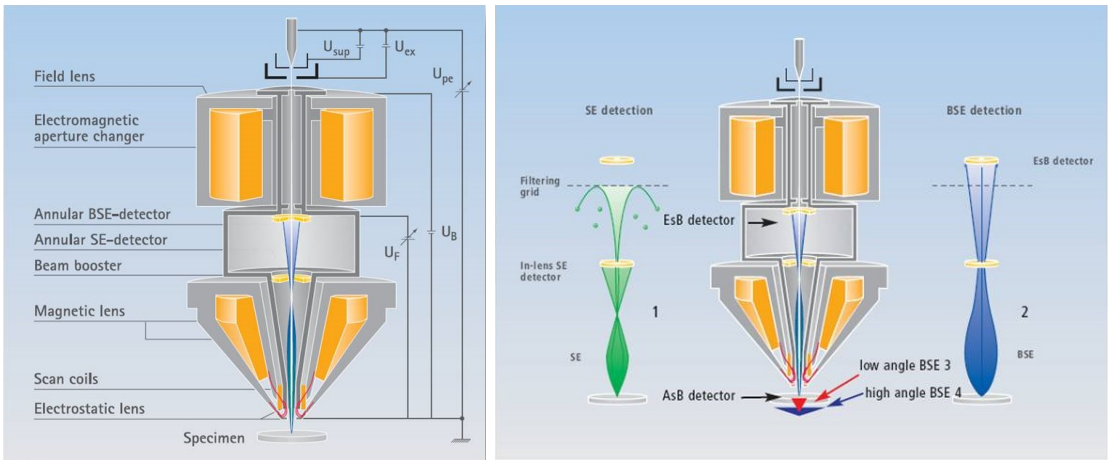

Figure 7.4: (A), Left: Bias concept of GEMINI "In-Lens" detector; (B)Right: Filter Grid and (1)secondary electron imaging, (2)pure high angle backscattered electron imaging, (3) low angle backscattered electron imaging; (4) high angle backscattered electron imaging[105]

tors)(Figure.7.4(B))[1]. In Nanoscience center, the Raith eline was equipped with " In-Lens secondary electron detector" and normal "secondary electron detector".
In this experiment, the target specimen are 5 nm gold particles, traditional backscattering detector (BSE-detector) and secondary electron detector (SE-detector) can not provide such high lateral resolution. For BS detector, most signal comes from 50 nm or deeper place under the surface, at this depth, the signal are all collected from silicon substrate. As for traditional SE detector, the main limit of detection comes from large divergent angle.

Further more, the so called "charging effect" and possible dirty vacuum system (even at high vacuum condition) will totally destroy the sample after long time espousing.

7.1.1 Self-assembly of AuNPs on silicon

Self assembly of gold particles has been widely researched for its application in opto-electronics, thermo-electronics, magnetic application and catalysis[44]. Two methods of preparation of these kinds of 2D superlattices include: adding a bad solvent and solvent evaporation method.

In this experiment, a total of 50 μ L biotinylated AuNPs with concentration of 4.5×10^{-6}mol/L was incubated on the surface for evaporation until totally dried. From Fig.7.1.1(A), AuNPs are evenly dislocated on the surface, with nearly perfect two dimensional structure. While, from Figure.7.1.1 (B), AuNPs were aggregated into

[1] http://www.raith.com/?xml=solutions%7CLithography+%26+nanoengineering%7Ce_LiNE+plus%7CElectron+detection+capabilities

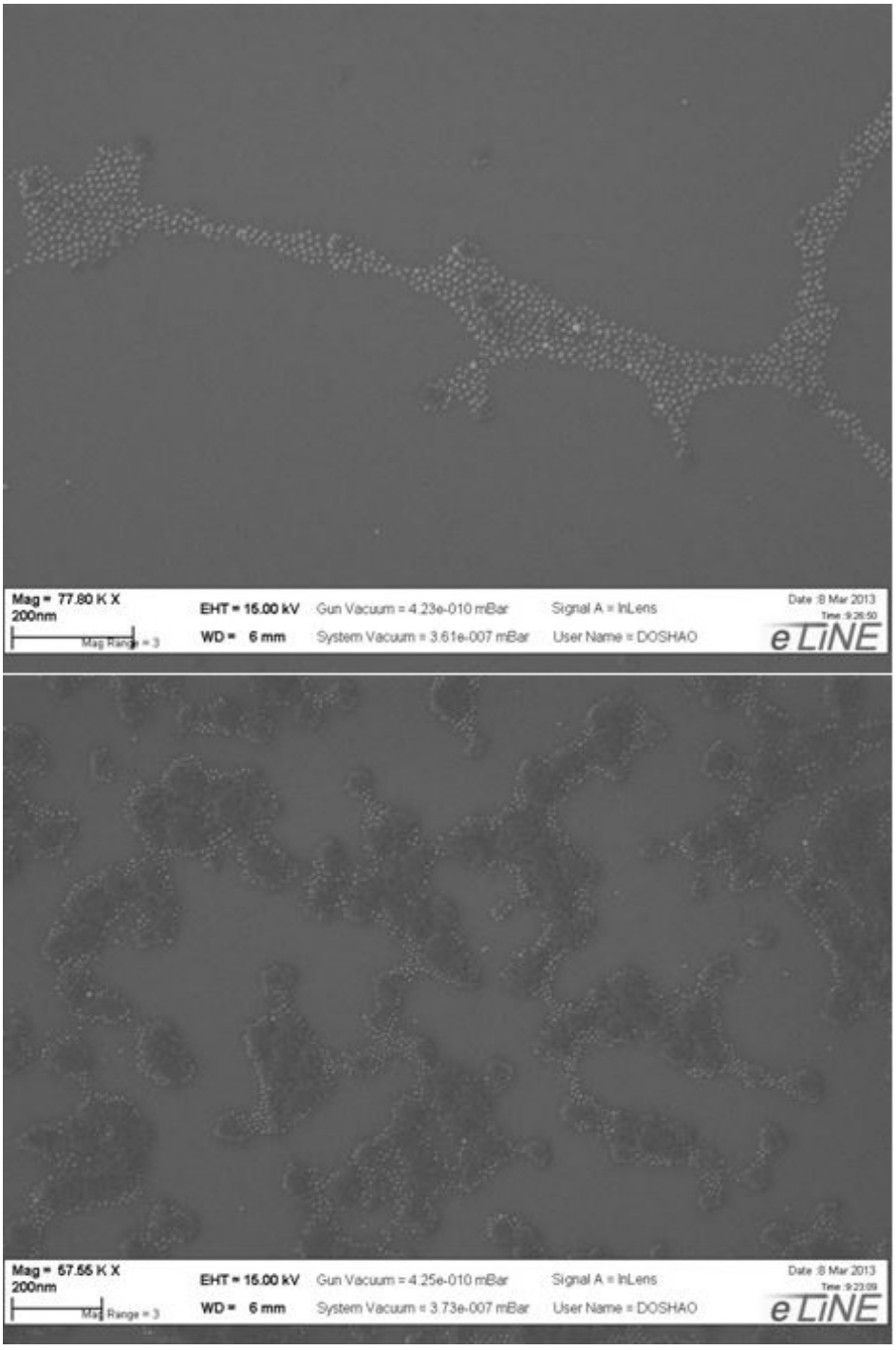

Figure 7.5: (A),2D monolayer of biotinylated gold particles on the surface of silicon;(B), AuNPs clusters with isolated gold particles at the edges

"islands", and at the edges of these "islands", we can see some isolated gold particles. This work is mainly helped by bachelor student Hannu Pasanen.
Another interesting property of biotinylated AuNPs self assembly monolayer, is they can be easily washed away by deionized water. This is very important for eliminating false signal of AuNPs that purely physical adsorption on the substrate.

7.2 Immobilization of proteins on the graphite

As it mentioned in the Chapter 5, protein immobilization can be done by both chemical and physical methods. In this section, only non-covalent method is used. Proteins' covalent immobilization on functionalized carbon nanotube are presented in next chapter.

Chimeric avidin [106](Institute of biomedical technology, University of Tampere) kept at -20 Celsius was diluted into 1ug/ml, 10ug/ml and 100ug/ml with phosphate buffered saline (PBS) at room temperature. They were separately incubated on the surface of graphite for 5 mins, and washed three times with deionized water.

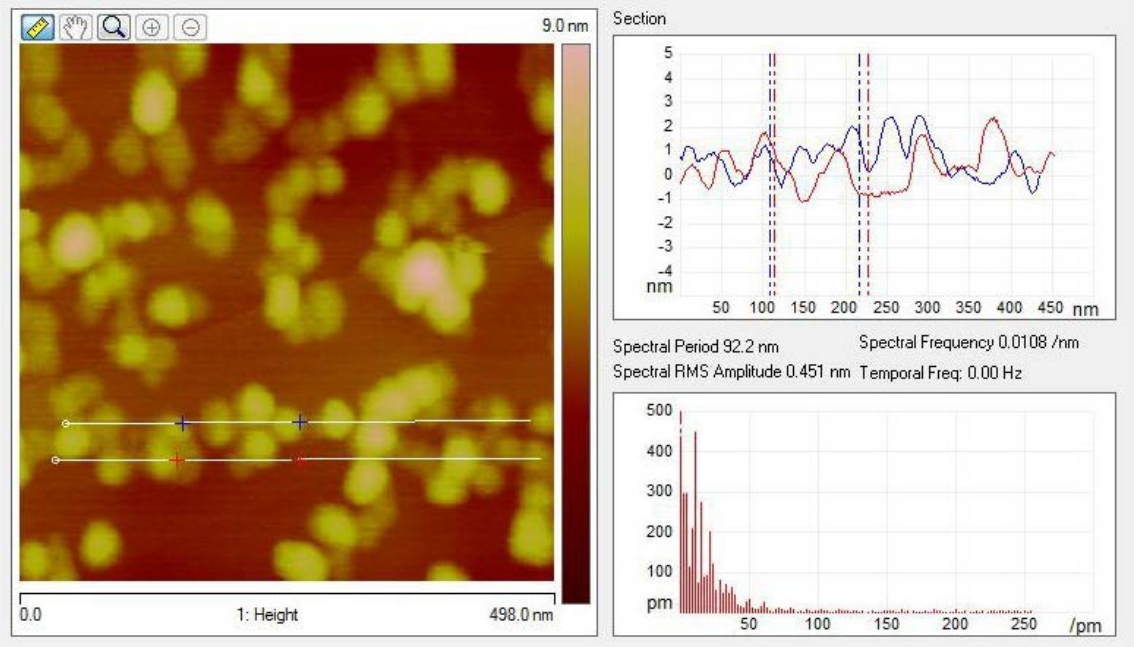

Figure 7.6: (A) Height data of separated 1ug/ml chimeric avidin incubation on graphite for 5 mins, scanning size $500nm \times 500nm$, on the right the section data of one line, the height of one single chimeric avidin is around 3 nm

From Fig.7.2 (A) and (B), it clearly showed that for low concentration (1ug/ml) chimeric avidins were distributed evenly on the surface.The height of one single chimeric avidin in dry condition varied from 2 to 3 nanometer, which is slight lower than X-ray

crystalline prediction. This experiment tells that even chimeric avidin has similar carbohydrate component as streptavidin, the non-covalent binding seems inevitable.

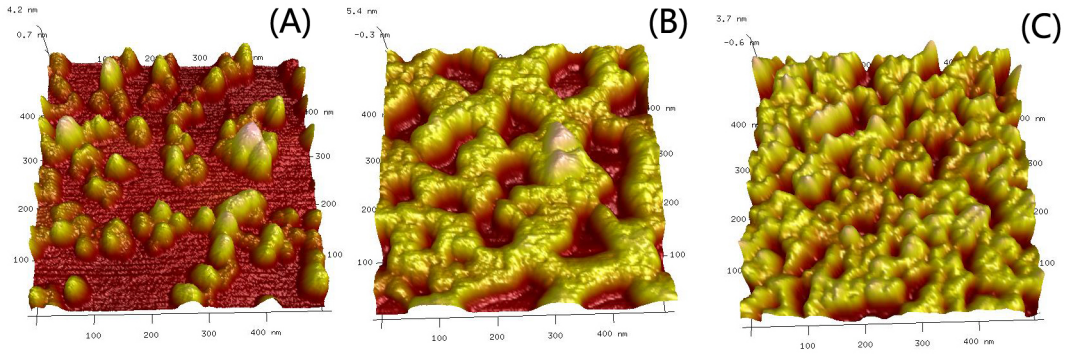

Figure 7.7: (A)3D image of 1ug/ml chimeric avidin on graphite (B) 3D image of 10ug/ml chimeric avidin on graphite; (C) 3D image of 100ug/ml chimeric avidin on graphite; scanning size= 500nm

Similarly method for another two different solution concentrations 10ug/ml and 100ug/ml chimeric avidin was also done on graphite. There images are shown in Figure.7.2 (B) and (C).

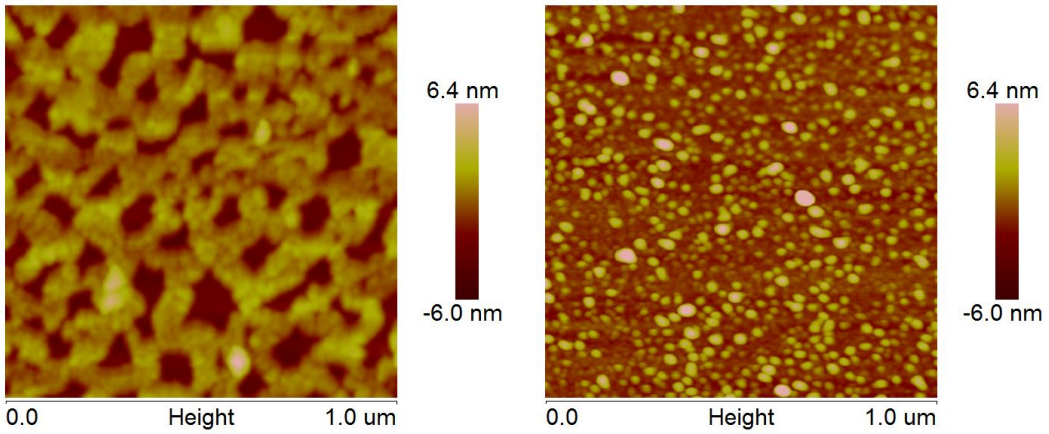

Figure 7.8: (A)5mins 10ug/ml chimeric avidin incubation on graphite with scanning size of 1 micrometer. Here obvious aggregation can be founded. (B) 20mins incubation of 10ug/ml streptavidin on surface of silicon where high density isolated streptavidin can be found, but no aggregation phenomena

Compared with different concentration of chimeric avidin's physical adsorption on graphite (Fig.7.2 (A)-(C)), it clearly showed that when chimeric avidin's concentration increase up to 10ug/ml, the protein was more likely to aggregated into monolayer (Fig.7.2(A)) on graphite. However, this is not the case for all the substrate. For silicon substrate, higher concentrated protein (Fig.7.2(D)) only increases the density of

separated proteins. One possible explanation is due to rigidly of silicon restrict the protein's movement.

Chapter 8

Functionalization of nanotubes with protein

8.1 Non-covalent immobilization of protein on carbon nanotube

Immobilization of protein on carbon nanotube and detection with biotinylated AuNPs is a assembly process. This assembly process can be naturally divided into three steps: carbon nanotube adsorption on silicon; protein immobilization on carbon nanotubes and biotinylated AuNPs specific binding with avidin. For the first two steps, I have already shown carbon nanotube deposition in Chapter. 6.4 and protein immobilization in Chapter. 7.2. So, in this section, I will not use tedious sentences to repeat these experimental steps.

One isolated single-walled carbon nanotube was scanning under AFM and SEM before and after non-covalent immobilization of chimeric avidin with the help of AFM markers. The single-walled carbon nanotube before streptavidin was recorded in Figure.8.1(A).

After fixation of carbon nanotube, the sample was immersed in 1ug/ml streptavidin solution for 20 mins based on Dai et al's method. The height changes before and after protein immobilization was then recorded by AFM (Fig.8.1(B)). Comparing with Figure.8.1(A) and Figure.8.1(B), we can clearly see that, streptavidin were located both on carbon nanotube and on silicon surface. The height variation before and after streptavidin incubation of carbon nanotube is a bit of trick to analyze, since protein will round the diameter of CNT that limits the accuracy of observation.

Immersed the sample immediately into the PBS for 1 hour in order to recover the protein's activity. After that biotinylated AuNPs was added to bind with streptavidin, and then transferred into scanning electron microscope for detection. The SEM result are shown in Fig.8.1. The intensity of biotinylated AuNPs was lower than protein's

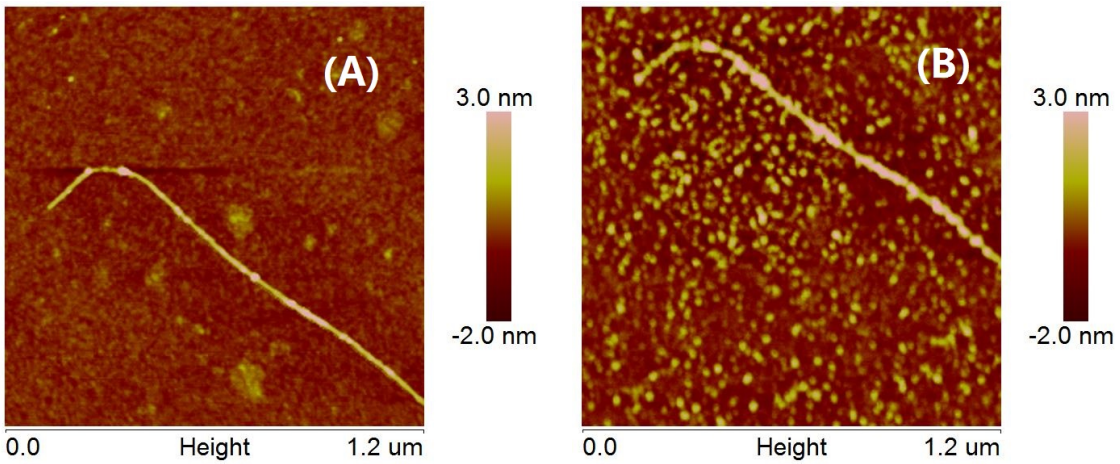

Figure 8.1: A,Single walled carbon nanotube on the silicon; B, Nonspecific adsorption of streptavidin on carbon nanotube

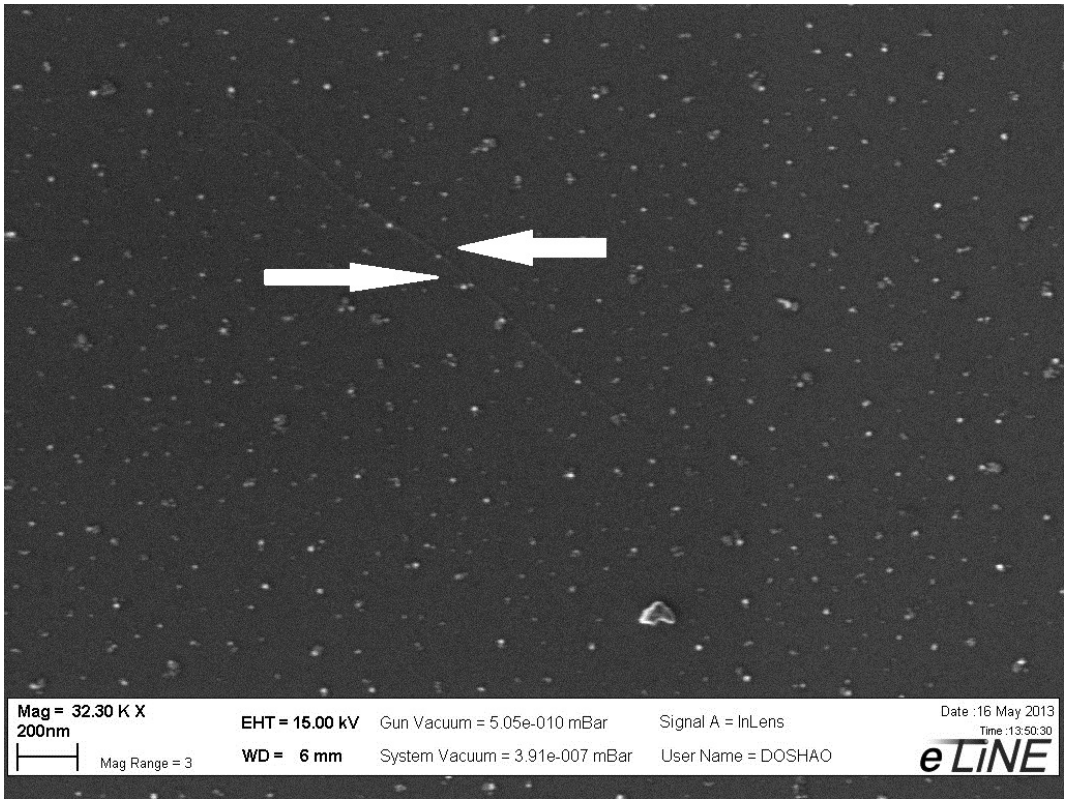

Figure 8.2: Scanning electron microscope of carbon nanotube with streptavidin and biotinylated AuNPs

density shown in AFM images. Two possible explanations are: (1) the process of AFM imaging of streptavidin immobilized carbon nanotube was in dry condition, some streptavidin may loss its activity during this process; (2) the streptavidin was nonspecific binding on the surface, the orientation of streptavidin was uncertain, the reaction part of protein may be hindered.

8.2 Covalent immobilization of protein on functionalized carbon nanotube

Covalent immobilization of protein on carbon nanotube is a kind of trick part of the whole experiment, because even without cross-linker, chimeric avidin will finally "gripe" carbon nanotube by hydrophobic interaction in the end. Some methods to eliminate this side interaction used in this experiment: (a), shorten incubation time, I change usually 20 minutes incubation period to 30 seconds; (b), wash the sample by deionized water several times to take away unstable binding protein.

8.2.1 Hydrogen peroxide treatment of carbon nanotube

Hydrogen peroxide treatment of multi-walled carbon nanotube and single-walled carbon nanotube's method was similar with hydrophilic treatment of graphite. The experiment results (Figure.8.3)shows that, after 45 minutes 35 percent hydrogen peroxide treatment, the carbon nanotube on silicon will not change its location. The height data of the same carbon nanotube (Figure.8.3(C)) shows the variation of carbon nanotube's height is in 1nm. Some possible explanation for this height changes may come from the destruction of MWCNT's outer shell.

The whole sample was then immersed in 1mg/ml 1-Ethyl-3-(3-dimethylaminopropyl) carbodimmide for 30 seconds, and then changed into 50mg/ml N-Hydroxysuccinimide solution. These two process are chemical reactions in order to form semi-stable reactive NHS ester (Details see Chapter 5.3.1 Covalent functionalization of carbon nanotube). After three times cleaning in deionized water, 10ug/ml chimeric avidin was added and incubated for 30 seconds, which should bind with NHS ester and form a peptide. Immediately washed the sample for three times and transfered it for AFM scanning.

Considering the phase image and height data image (Fig.8.4) of covalent immobilization, we can clearly see the "necklace" structure. Here, the "jewelleris" made of chimeric avidin locate along the "string" composed by carbon nanotube. But this is not a conclusive result of a successful covalent binding of protein on NHS ester groups on carbon nanotube. If we compare Fig.8.4(B) to and Fig.8.4(C), we can clearly see

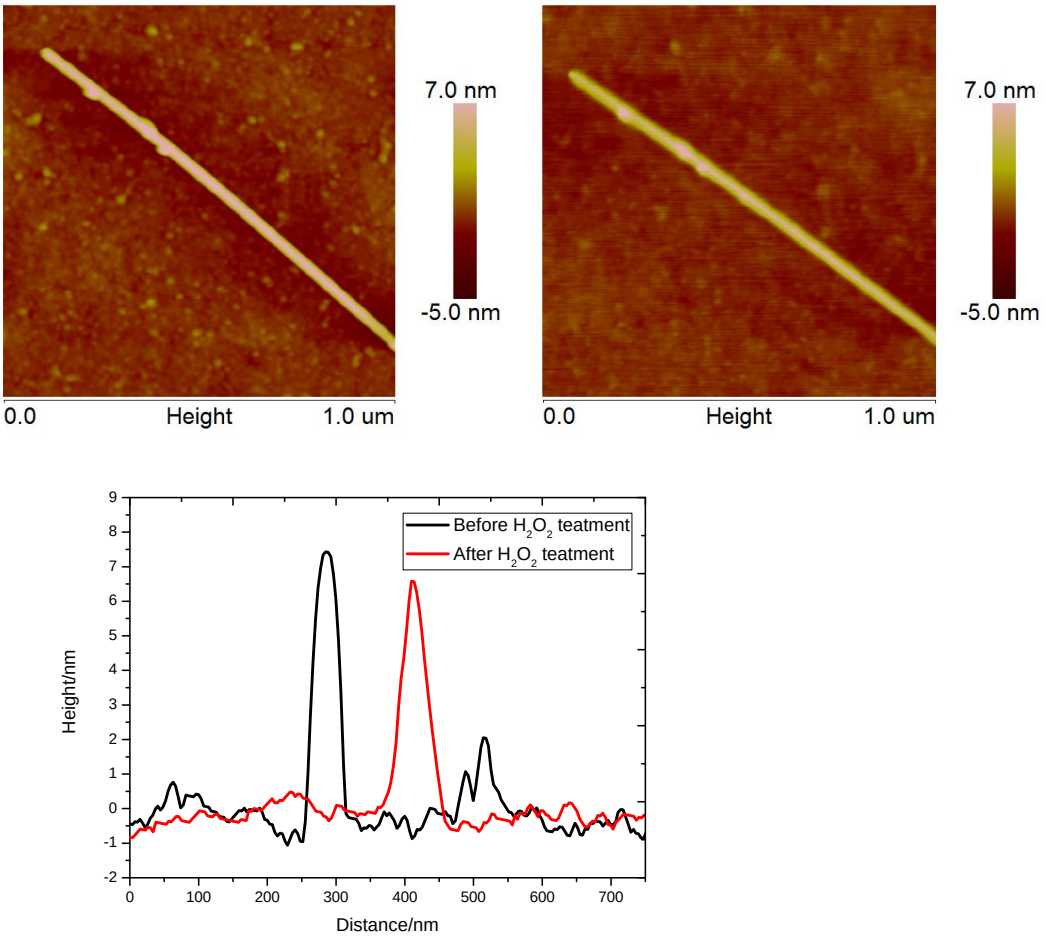

Figure 8.3: (A) Multi-walled carbon nanotube before hydrogen peroxide treatment; (B) The same multi-walled carbon nanotube after hydrogen peroxide treatment; data scale of -5nm to 7nm

the "relative height changes" of carbon nanotube, which is caused by covalent binding of protein on the silicon NHS ester surface. Hydrogen peroxide solution has strong oxidation property, it can not only oxidize reactive carbon atoms on carbon nanotube, but also silicon surface at the same time. This hydroxyl group functionalized by hydrogen peroxide did the same reaction with EDAC and NHS, which made this carbon nanotube finally immersed in the sea of protein. But, in general, this is a promising experiment, and further research is being considered.

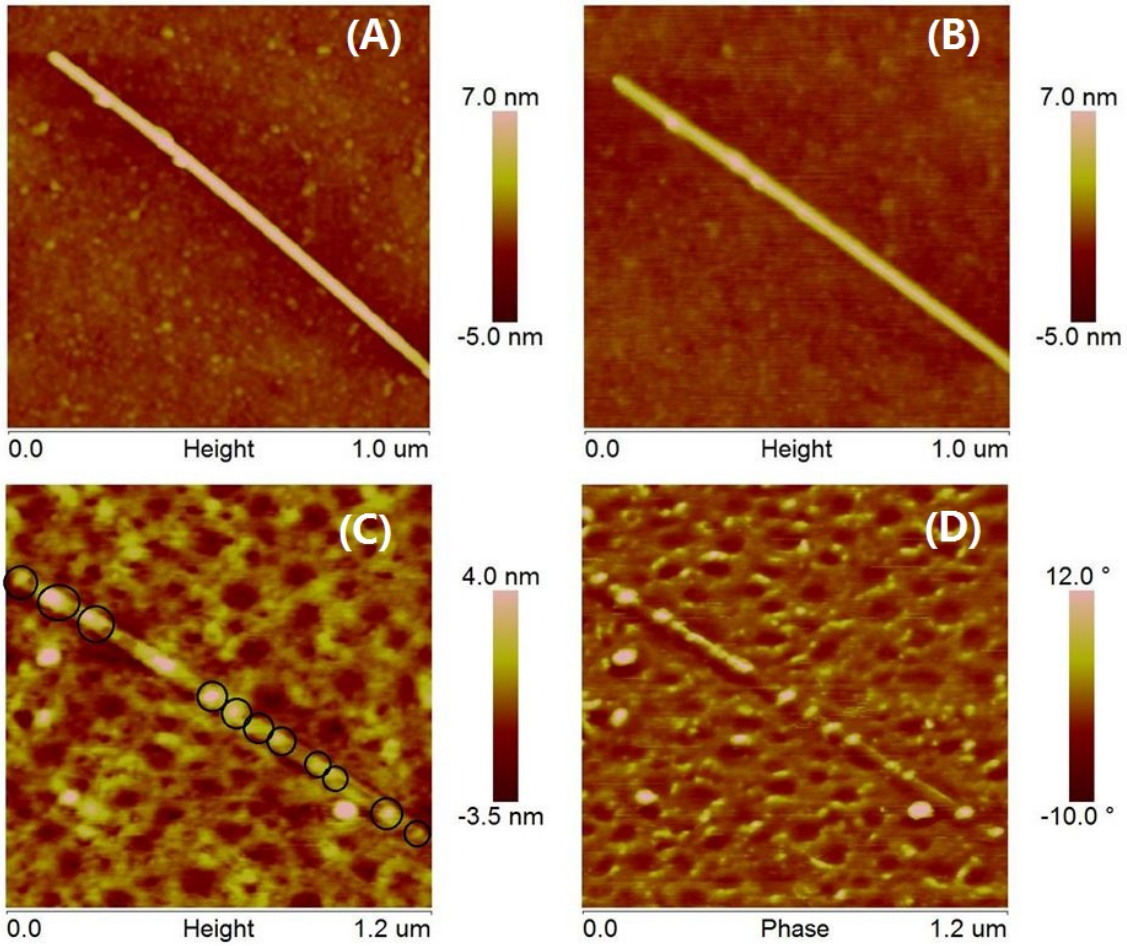

Figure 8.4: (A), Multiwalled carbon nanotube before hydrogen peroxide treatment; (B), After hydrogen peroxide treatment, the location of multiwalled carbon nanotube stay the same; (C), Height image of protein immobilization, the black circle indicates protein's location; (D)Phase image of protein immobilization, can we can clearly see the protein " jewelleris"along carbon nanotube "necklace" structure

Chapter 9

Summary

Carbon nanotube based next generation "point of care" biosensor has attracted more and more researcher's attention due to its unique theoretical and practical application. It is such an interesting and a bit of complicated research area, that a systematic study seems very unlikely to finish in just a two year's master degree study. Therefore, further research will carry on based on the current research results.

In this master degree period, I first tried to detect and observe in practise carbon nanotube based biosensor's individual components, such as protein, substrates, gold nanoparticles etc. In the final part, I assembled one simple sample to test its validity on silicon. From these testing results, I think it is not too farreaching to draw the following two conclusions: (A) hydrogen peroxide treatment is one possible methods to functionalized multiwalled carbon nanotubes; (B) using NHS-EDAC two steps binding, we may get a covalent linking chimeric avidin to functionalized carbon nanotube.

For further research, more quantity testing system with more controllable and repeatable methods will be included, which should give us more conclusive result.

Part III

Appendix

Chapter 10

Supramolecular chemistry

From history view of nanotechnology and nanoscience, it is very clear that some of the most original and basics ideas such as "bottom up principle"[107], "self assembly"[107], "molecular machinery"[108] are all very firmly related to "non-covalent interaction" or supramolecular chemistry[109].

10.0.2 Primary bonding and secondary bonding

Table 10.1: Bond strength of different primary and secondary bonding

Types of interaction bondings	Bond strength
Ionic bonds	600 kJ/mol to 16,000 kJ/mol
Covalent bonds	200 kJ/mol to 1000 kJ/mol
Metallic bonds	60 kJ/mol to 800 kJ/mol
avidin - biotin	107.6 kJ/mol[10]
chimeric avidin- biotin	112.6 kJ/mol[10]
Ion-dipole interaction	50 to 200 kJ/mol
Dipole-dipole interaction	5 to 50 kJ/mol
Hydrogen bonding	4 to 120 kJ/mol
π- π interaction	8-12 kJ/mol
Van der Waals interaction	0.4 to 4 kJ/mol
Hydrophobic interaction	about 2.5 kJ/mol

Unlike the definition in physics, strong interaction (primary bonding) between atoms include ionic, covalent, metallic bonds. And usually the energy of these bonds (above 100 kJ/mol) are far too high than thermal energy at room temperature (2.5 kJ/mol) that can not be broken by temperature[110]. Instead of strong interaction, supramolecular chemistry deal with non-covalent interactions (5 to 80 kJ/mol) like ion-dipole, dipole-dipole, hydrogen, π-π, Van der Waals forces, and hydrophobic interactions. Since the energy of secondary bonding is much more similar with thermal energy, it is possible

to only break secondary bonding (sonication, heating etc) while leaves alone primary bonding under laboratory condition (see Table 10.1).

Chapter 11

Facilities used in the experiments

11.1 Confocal microscope

Microscopes is an widely used research facility date back to 17th century, and have played a fundamental role in modern science's development[111]. The confocal microscope used in this experiment was Olympus Fluoview 1000, for dark field image, the microscope used was Olympus BX51M. Some parameters of Olympus Fluoview 1000 confocal microscope is list in the Table.11.1

Table 11.1: Microscope settings

Parameter	Settings
Microscope	Olympus IX81
Confocal	Olympus FluoView 1000
Laserlines	488nm (argon), 543nm (HeNe), 633nm (HeNe)
Objective	UpLSAPO 60x oil (NA=1.35)
Filters	500-530nm, 570-640nm, 650nm long pass filter
Image size	640× 640 pixels

11.2 Scanning electron microscope

Ernst Ruska and Max Knoll in early 1930s built the first transmission electron microscope to overcome the "Ernst Abbe's theoretical resolution limit", which extended the microscope's resolution to nanoscale[112].

In this master thesis, scanning electron microscope used was Raith e-Line which was designed for electron beam lithography (feature size less than 20nm) and high resolution SEM imaging. Some key specification of Raith e-line was list in the Table

Table 11.2: Raith Eline's parameters from Nanoscience Center

Properties	Measured
Filament	Schottky thermal field emission source
Beam size	1.8nm 20 keV
	3.5nm 1 keV
Beam current range	5 pA- 20 nA
Beam energy	100 eV - 30 keV
Min.feature size	18.2 nm line

And besides normally secondary electron detector (Everhart-Thornley detector), Raith Eline also includes one "in lens" electron detector which explains the high lateral resolution images of gold particles and carbon nanotube in this paper (see `https://www.raith.com`).

11.3 Scanning force microscope

In early 1980's G.Binning invented the scanning probe micrsocopy[113] that provided a new method not only see but manipulate nanoscale oject[111].Scanning force microscopy is a high resolution imaging facility, in vertical direction, the accuracy of scanning force microscopy can be as high as 0.1Å[114]. Another distinguished property of scanning force microscope is that they can work in different environments, from ultrahigh vacuum to liquid condition. And now scanning force microscopies has been widely used in biology and materials science[115].

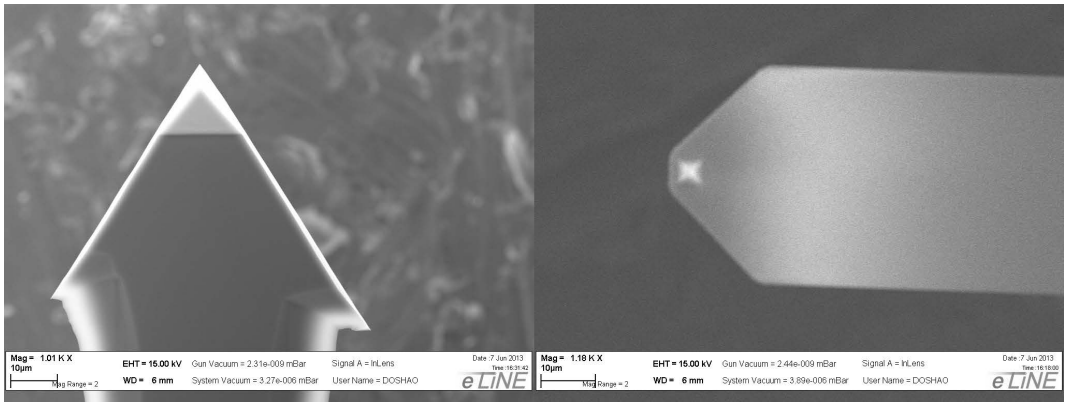

Figure 11.1: (A), Arrow NCR probe cantilever; (B), Long PNP-DB-20 contact tip

In this master thesis, the scanning force microscope used are Digital Instruments, Dimension 3100 (NanoScope IV) and (Nanoscope V). And the software to analyze data is Bruker NanoScope Analysis 1.40. Without specific mention, the tips used in

this experiment are: Aspire CT 300 Conical Tapping Mode AFM Probes [1] and Arrow NCR probes (Fig.11.1(A)) for tapping mode in dry condition [2]. And for liquid tapping mode and liquid contact mode, PNP-DB-20 (Fig.11.1(B)) from Nanoworld were used[3]. All these tips are guaranteed with typically tip radius less than 10 nm.

11.4 Physical vapor deposition

In this experiment, ultra high vacuum (UHV) evaporator supplied by Instrumentti Mattila Oy manufactured in 1998. This instrument can used for deposition metals with pressure of 10^{-8} mbar [4]. Based on kinetic theory of molecule, the mean free path (MFP) can be calculated as

$$\lambda_{MFP} = \frac{K_B T}{\sqrt{2} P \pi d^2} \tag{11.1}$$

where K_B = Boltzmann constant, T= temperature, P=pressure, d=diamter of molecule. Considering gold atom used in this experiment at room temperature (300K), the mean free path is far beyond the diameter of UHV chamber. So all the trajectories can be seen as ballistic.

11.5 RIE/CVD

Reactive ion etching instrument used in this experiment is Oxford Instruments Plasmalab 80 plus PECVD + RIE[5]. Available gas include Ar, O_2, SF_6 and CHF_3. The working temperature vary from -150 degree to +400 degree.

[1] `https://http://www.nanoscience.com/index.html`
[2] `http://www.nanoworld.com/tapping-mode-reflex-coated-afm-tip-arrow-ncr`
[3] http://www.nanoworld.com/pyrex-nitride-rectangular-silicon-nitride-cantilever-afm-tip-pnp-db
[4] `http://www.instrumentti-mattila.fi/home.html`
[5] `http://www.oxfordplasma.de/systems/80plus.htm`

Bibliography

[1] Neil A.Campbell et al. *Biology 8th edition*. Pearson Press, 2008.

[2] Ram Weiss, James Dziura, Tania S. Burgert, William V. Tamborlane, Sara E. Taksali, Catherine W. Yeckel, Karin Allen, Melinda Lopes, Mary Savoye, John Morrison, Robert S. Sherwin, and Sonia Caprio. Obesity and the metabolic syndrome in children and adolescents. *New England Journal of Medicine*, 350(23):2362–2374, 2004. PMID: 15175438.

[3] Franoise Imbert-Bismut, Vlad Ratziu, Laurence Pieroni, Frederic Charlotte, Yves Benhamou, and Thierry Poynard. Biochemical markers of liver fibrosis in patients with hepatitis c virus infection: a prospective study. *The Lancet*, 357(9262):1069 – 1075, 2001.

[4] Thermo Science Company. *Thermo Scientific Avidin-Biotin Technical Handbook*.

[5] Meir Wilchek Oded Livnah, Edward A.Bayer. Three dimensional structures of avidin and the avidin-biotin complex. *Proc.Natl.Acad.Sci. USA*, 90:5076–5080, June 1993.

[6] Lasse Valimaa. *Streptavidin- A versatile binding perotein for solid phase immunoassays*. PhD thesis, University of Turku, 2008.

[7] Isolde Le Trong, Zhizhi Wang, David E. Hyre, Terry P. Lybrand, Patrick S. Stayton, and Ronald E. Stenkamp. Streptavidin and its biotin complex at atomic resolution. *ACTA CRYSTALLOGRAPHICA SECTION D-BIOLOGICAL CRYSTALLOGRAPHY*, 67(9):813–821, SEP 2011.

[8] VR Hytonen, OIH Laitinen, TT Airenne, H Kidron, NJ Meltola, EJ Porkka, J Horha, T Paldanius, JAE Maatta, HR Nordlund, MS Johnson, TA Salminen, KJ Airenne, S Yla-Herttuala, and MS Kulomaa. Efficient production of active chicken avidin using a bacterial signal peptide in Escherichia coli. *BIOCHEMICAL JOURNAL*, 384(2):385–390, DEC 1 2004.

[9] Rob P H Kooyman, Robert M Corn, Alastair Wark, Hye Jin Lee, Erk Gedig, Gerard Engbers, Lennart Walstrom, Nico J de Mol, Damien R Hall, Paul Yager,

Timothy Chinowsky, Elain Fu, Kjell Nelson, Alan McWhirter, Marcel J E Fischer, Angelique M C Lokate, J Bianca Beusink, Ger J M Pruijn, Wolfgang Knoll, Amal Kasry, Jing Liu, Thomas Neumann, Lifang Niu, Hyeyoung Park, Harald Paulsen, Rudolf Robelek, Fang Yu, and Peter Schuck. *Handbook of Surface Plasmon Resonance*. The Royal Society of Chemistry.

[10] Juha A. E. Maatta, Yael Eisenberg-Domovich, Henri R. Nordlund, Ruchama Hayouka, Markku S. Kulomaa, Oded Livnah, and Vesa P. Hytonen. Chimeric Avidin Shows Stability Against Harsh Chemical Conditions-Biochemical Analysis and 3D Structure. *BIOTECHNOLOGY AND BIOENGINEERING*, 108(3):481–490, MAR 2011.

[11] Bhaswati Barat and Anna M. Wu. Metabolic biotinylation of recombinant antibody by biotin ligase retained in the endoplasmic reticulum. *BIOMOLECULAR ENGINEERING*, 24(3):283–291, SEP 2007.

[12] Jay Nadeau. *Introduction to Experimental Biophysics: Biological Methods for Physical Scientists*. CRC Press, 2011.

[13] C Rosano, P Arosio, and M Bolognesi. The X-ray three-dimensional structure of avidin. *BIOMOLECULAR ENGINEERING*, 16(1-4):5–12, DEC 31 1999.

[14] RJ Chen, YG Zhang, DW Wang, and HJ Dai. Noncovalent sidewall functionalization of single-walled carbon nanotubes for protein immobilization. *JOURNAL OF THE AMERICAN CHEMICAL SOCIETY*, 123(16):3838–3839, APR 25 2001.

[15] M Shim, NWS Kam, RJ Chen, YM Li, and HJ Dai. Functionalization of carbon nanotubes for biocompatibility and biomolecular recognition. *NANO LETTERS*, 2(4):285–288, APR 2002.

[16] CK Riener, CM Stroh, A Ebner, C Klampfl, AA Gall, C Romanin, YL Lyubchenko, P Hinterdorfer, and HJ Gruber. Simple test system for single molecule recognition force microscopy. *ANALYTICA CHIMICA ACTA*, 479(1):59–75, MAR 5 2003.

[17] Young-Soon Kim, Joong-Hee Cho, S. G. Ansari, Hyung-Il Kim, M. A. Dar, Hyung-Kee Seo, Gil-Sung Kim, Dai-Soo Lee, Gilson Khang, and Hyung-Shik Shin. Immobilization of avidin on the functionalized carbon nanotubes. *SYNTHETIC METALS*, 156(14-15):938–943, JUL 1 2006.

[18] S MIYAMOTO and PA KOLLMAN. ABSOLUTE AND RELATIVE BINDING FREE-ENERGY CALCULATIONS OF THE INTERACTION OF BIOTIN AND ITS ANALOGS WITH STREPTAVIDIN USING MOLECULAR-

DYNAMICS FREE-ENERGY PERTURBATION APPROACHES. *PROTEINS-STRUCTURE FUNCTION AND GENETICS*, 16(3):226–245, JUL 1993.

[19] M Gonzalez, LA Bagatolli, I Echabe, JLR Arrondo, CE Argarana, CR Cantor, and GD Fidelio. Interaction of biotin with streptavidin - Thermostability and conformational changes upon binding. *JOURNAL OF BIOLOGICAL CHEMISTRY*, 272(17):11288–11294, APR 25 1997.

[20] S. Iijima. Helical microtubules of graphitic carbon. *Nature*, 354:56–58, November 1991.

[21] S IIJIMA and T ICHIHASHI. SINGLE-SHELL CARBON NANOTUBES OF 1-NM DIAMETER. *NATURE*, 363(6430):603–605, JUN 17 1993.

[22] Marc Monthioux and Vladimir L. Kuznetsov. Who should be given the credit for the discovery of carbon nanotubes? *CARBON*, 44(9):1621–1623, AUG 2006.

[23] L.V. Radushkevich and V.M. Lukyanovich. O strukture ugleroda, obrazujucegosja pri termiceskom razlozenii okisi ugleroda na zeleznom kontakte. *Zurn. Fisic. Chim*, 26:88–95, 1952.

[24] SS Wong, E Joselevich, AT Woolley, CL Cheung, and CM Lieber. Covalently functionalized nanotubes as nanometre-sized probes in chemistry and biology. *NATURE*, 394(6688):52–55, JUL 2 1998.

[25] Bin Kang, Decai Yu, Yaodong Dai, Shuquan Chang, Da Chen, and Yitao Ding. Biodistribution and accumulation of intravenously administered carbon nanotubes in mice probed by raman spectroscopy and fluorescent labeling. *Carbon*, 47(4):1189 – 1192, 2009.

[26] Lingjie Meng, Xiaoke Zhang, Qinghua Lu, Zhaofu Fei, and Paul J. Dyson. Single walled carbon nanotubes as drug delivery vehicles: Targeting doxorubicin to tumors. *Biomaterials*, 33(6):1689 – 1698, 2012.

[27] SS Fan, MG Chapline, NR Franklin, TW Tombler, AM Cassell, and HJ Dai. Self-oriented regular arrays of carbon nanotubes and their field emission properties. *SCIENCE*, 283(5401):512–514, JAN 22 1999.

[28] John McMurry. *Fundamentals of Organic Chemistry*. Mary Finch, 2011.

[29] Peng-Cheng Ma, Naveed A. Siddiqui, Gad Marom, and Jang-Kyo Kim. Dispersion and functionalization of carbon nanotubes for polymer-based nanocomposites: A review. *COMPOSITES PART A-APPLIED SCIENCE AND MANUFACTURING*, 41(10):1345–1367, OCT 2010.

[30] Mark Oliver Goerbig Jean-Noel Fuchs. Introduction to the physical properties of graphene, 2008.

[31] Christian Schonenberger. Bandstructure of graphene and carbon nanotubes: An exercise in condensed matter physics, April 2000.

[32] G. Dresselhaus M. Dresselhaus and P. Eklund. *Science of Fullerenes and Carbon Nanotubes*. Academic Press, 1996.

[33] Ethan Davis Minot. *TUNING THE BAND STRUCTURE OF CARBON NANOTUBES*. PhD thesis, Cornell University, 2004.

[34] M.MEYYAPPAN. *CARBON NANOTUBES SCIENCE AND APPLICATIONS*. CRC PRESS, 2005.

[35] DH ROBERTSON, DW BRENNER, and JW MINTMIRE. ENERGETICS OF NANOSCALE GRAPHITIC TUBULES. *PHYSICAL REVIEW B*, 45(21):12592–12595, JUN 1 1992.

[36] JW MINTMIRE and CT WHITE. ELECTRONIC AND STRUCTURAL-PROPERTIES OF CARBON NANOTUBES. *CARBON*, 33(7):893–902, 1995.

[37] Weiwei Zhou, Lei Ding, Sungwoo Yang, and Jie Liu. Synthesis of High-Density, Large-Diameter, and Aligned Single-Walled Carbon Nanotubes by Multiple-Cycle Growth Methods. *ACS NANO*, 5(5):3849–3857, MAY 2011.

[38] HW KROTO, JR HEATH, SC OBRIEN, RF CURL, and RE SMALLEY. C-60 - BUCKMINSTERFULLERENE. *NATURE*, 318(6042):162–163, 1985.

[39] A. K. Geim and K. S. Novoselov. The rise of graphene. *NATURE MATERIALS*, 6(3):183–191, MAR 2007.

[40] MC Daniel and D Astruc. Gold nanoparticles: Assembly, supramolecular chemistry, quantum-size-related properties, and applications toward biology, catalysis, and nanotechnology. *CHEMICAL REVIEWS*, 104(1):293–346, JAN 2004.

[41] F Caruso, M Spasova, V Saigueirino-Maceira, and LM Liz-Marzan. Multilayer assemblies of silica-encapsulated gold nanoparticles on decomposable colloid templates. *ADVANCED MATERIALS*, 13(14):1090+, JUL 18 2001.

[42] Jeffrey N. Anker, W. Paige Hall, Olga Lyandres, Nilam C. Shah, Jing Zhao, and Richard P. Van Duyne. Biosensing with plasmonic nanosensors. *NATURE MATERIALS*, 7(6):442–453, JUN 2008.

[43] T Endo, K Kerman, N Nagatani, Y Takamura, and E Tamiya. Label-free detection of peptide nucleic acid-DNA hybridization using localized surface plasmon resonance based optical biosensor. *ANALYTICAL CHEMISTRY*, 77(21):6976–6984, NOV 1 2005.

[44] D. Vanmaekelbergh. Self-assembly of colloidal nanocrystals as route to novel classes of nanostructured materials. *NANO TODAY*, 6(4):419–437, AUG 2011.

[45] J TURKEVICH, PC STEVENSON, and J HILLIER. A STUDY OF THE NUCLEATION AND GROWTH PROCESSES IN THE SYNTHESIS OF COLLOIDAL GOLD. *DISCUSSIONS OF THE FARADAY SOCIETY*, (11):55–&, 1951.

[46] M BRUST, M WALKER, D BETHELL, DJ SCHIFFRIN, and R WHYMAN. SYNTHESIS OF THIOL-DERIVATIZED GOLD NANOPARTICLES IN A 2-PHASE LIQUID-LIQUID SYSTEM. *JOURNAL OF THE CHEMICAL SOCIETY-CHEMICAL COMMUNICATIONS*, (7):801–802, APR 7 1994.

[47] T Yonezawa and T Kunitake. Practical preparation of anionic mercapto ligand-stabilized gold nanoparticles and their immobilization. *COLLOIDS AND SURFACES A-PHYSICOCHEMICAL AND ENGINEERING ASPECTS*, 149(1-3):193–199, APR 15 1999. 9th International Conference on Surface and Colloid Science (9ICSCS), SOFIA, BULGARIA, JUL 06-12, 1997.

[48] L Sun, RM Crooks, and V Chechik. Preparation of polycyclodextrin hollow spheres by templating gold nanoparticles. *CHEMICAL COMMUNICATIONS*, (4):359–360, 2001.

[49] LH DUBOIS and RG NUZZO. SYNTHESIS, STRUCTURE, AND PROPERTIES OF MODEL ORGANIC-SURFACES. *ANNUAL REVIEW OF PHYSICAL CHEMISTRY*, 43:437–463, 1992.

[50] Shuwen Zeng, Ken-Tye Yong, Indrajit Roy, Xuan-Quyen Dinh, Xia Yu, and Feng Luan. A Review on Functionalized Gold Nanoparticles for Biosensing Applications. *PLASMONICS*, 6(3):491–506, SEP 2011.

[51] Xiaohua Huang, Prashant K. Jain, Ivan H. El-Sayed, and Mostafa A. El-Sayed. Gold nanoparticles: interesting optical properties and recent applications in cancer diagnostic and therapy. *NANOMEDICINE*, 2(5):681–693, OCT 2007.

[52] R.W Wood. On a remarkable case of uneven distribution of light in a diffraction grating spectrum. *Philysophical magazine*, 4:396–402, 1902.

[53] Helmuth Horvath. Gustav Mie and the scattering and absorption of light by particles: Historic developments and basics. *JOURNAL OF QUANTITATIVE SPECTROSCOPY & RADIATIVE TRANSFER*, 110(11):787–799, JUL 2009. Annual Meeting of the Association-for-Aerosol-Research, Karlsruhe, GERMANY, JUL 03-04, 2008.

[54] Lord Rayleigh. Dynamical theory of the grating. *Proc.Roy.Soc.*, 79:399, 1907.

[55] C. H Palmer. Parallel diffraction grating anomalies. *J.Opt.Soc.Am*, 42:269, 1952.

[56] E. Kretschmann and H Reather. Radiative decay of nonradiative surface plasmon excited by light. *Z.Naturf*, 23A:2135–2136, 1968.

[57] A Otto. Exitation of nonradiative surface plasma waves in silver by the method of frustrated total reflection. *Z Phys*, 216:398–410, 1968.

[58] B LIEDBERG, C NYLANDER, and I LUNDSTROM. SURFACE-PLASMON RESONANCE FOR GAS-DETECTION AND BIOSENSING. *SENSORS AND ACTUATORS*, 4(2):299–304, 1983.

[59] WD Wilson. Analyzing biomolecular interactions. *SCIENCE*, 295(5562):2103+, MAR 15 2002.

[60] www.britishmuseum.org.

[61] Katherine A. Willets and Richard P. Van Duyne. Localized surface plasmon resonance spectroscopy and sensing. *ANNUAL REVIEW OF PHYSICAL CHEMISTRY*, 58:267–297, 2007.

[62] DR Thevenot, K Toth, RA Durst, and GS Wilson. Electrochemical biosensors: recommended definitions and classification. *BIOSENSORS & BIOELECTRONICS*, 16(1-2):121–131, JAN 2001.

[63] Yujun Song, Yuanqing Zhang, Paul E. Bernard, James M. Reuben, Naoto T. Ueno, Ralph B. Arlinghaus, Youli Zu, and Lidong Qin. Multiplexed volumetric bar-chart chip for point-of-care diagnostics. *NATURE COMMUNICATIONS*, 3, DEC 2012.

[64] Jonas Ljungblad. Antibody-conjugated gold nannoparticles integraed in a fluorescence based biochip. Master's thesis, Univeristy of Linkoping, 2009.

[65] J Wang. Electrochemical biosensors: Towards point-of-care cancer diagnostics. *BIOSENSORS & BIOELECTRONICS*, 21(10):1887–1892, APR 15 2006.

[66] Guodong Liu and Yuehe Lin. Nanomaterial labels in electrochemical immunosensors and immunoassays. *TALANTA*, 74(3):308–317, DEC 15 2007.

[67] Yongki Choi, Issa S. Moody, Patrick C. Sims, Steven R. Hunt, Brad L. Corso, Israel Perez, Gregory A. Weiss, and Philip G. Collins. Single-Molecule Lysozyme Dynamics Monitored by an Electronic Circuit. *Science*, 335(6066):319–324, January 2012.

[68] Kuan-I Chen, Bor-Ran Li, and Yit-Tsong Chen. Silicon nanowire field-effect transistor-based biosensors for biomedical diagnosis and cellular recording investigation. *Nano Today*, 6(2):131 – 154, 2011.

[69] J Kong, NR Franklin, CW Zhou, MG Chapline, S Peng, KJ Cho, and HJ Dai. Nanotube molecular wires as chemical sensors. *SCIENCE*, 287(5453):622–625, JAN 28 2000.

[70] Y Cui, QQ Wei, HK Park, and CM Lieber. Nanowire nanosensors for highly sensitive and selective detection of biological and chemical species. *SCIENCE*, 293(5533):1289–1292, AUG 17 2001.

[71] Xiuyun Wang and Shunichi Uchiyama. *Polymers for Biosensors Construction, State of the Art in Biosensors - General Aspects*. InTech, 2013.

[72] Pierce Biotechnology, Inc. *Crosslinking Reacgents Technical Handbook*, 2006.

[73] L Valentini, I Armentano, JM Kenny, C Cantalini, L Lozzi, and S Santucci. Sensors for sub-ppm NO2 gas detection based on carbon nanotube thin films. *APPLIED PHYSICS LETTERS*, 82(6):961–963, FEB 10 2003.

[74] K. Jensen, Kwanpyo Kim, and A. Zettl. An atomic-resolution nanomechanical mass sensor. *NATURE NANOTECHNOLOGY*, 3(9):533–537, SEP 2008.

[75] PW Barone, S Baik, DA Heller, and MS Strano. Near-infrared optical sensors based on single-walled carbon nanotubes. *NATURE MATERIALS*, 4(1):86–U16, JAN 2005.

[76] Peerapong Yotprayoonsak, Konsta Hannula, Tanja Lahtinen, Markus Ahlskog, and Andreas Johansson. Liquid-phase alkali-doping of individual carbon nanotube field-effect transistors observed in real-time. *CARBON*, 49(15):5283–5291, DEC 2011.

[77] David S. Hecht, Robert J. A. Ramirez, Mikhail Briman, Erika Artukovic, Kelly S. Chichak, J. Fraser Stoddart, and George Gruener. Bioinspired detection of light using a porphyrin-sensitized single-wall nanotube field effect transistor. *NANO LETTERS*, 6(9):2031–2036, SEP 13 2006.

[78] WG Kuhr. Electrochemical DNA analysis comes of age. *NATURE BIOTECHNOLOGY*, 18(10):1042–1043, OCT 2000.

[79] Phaedon Avouris, Zhihong Chen, and Vasili Perebeinos. Carbon-based electronics. *Nature Nanotechnology*, 2(10):605–15, 10 2007.

[80] J Svensson, Yu Tarakanov, D S Lee, J M Kinaret, Y W Park, and E E B Campbell. A carbon nanotube gated carbon nanotube transistor with 5ps gate delay. *Nanotechnology*, 19(32):325201, 2008.

[81] S Reich, L Li, and J Robertson. Structure and formation energy of carbon nanotube caps. *PHYSICAL REVIEW B*, 72(16), OCT 2005.

[82] H Hu, P Bhowmik, B Zhao, MA Hamon, ME Itkis, and RC Haddon. Determination of the acidic sites of purified single-walled carbon nanotubes by acid-base titration. *CHEMICAL PHYSICS LETTERS*, 345(1-2):25–28, SEP 7 2001.

[83] KY Jiang, LS Schadler, RW Siegel, XJ Zhang, HF Zhang, and M Terrones. Protein immobilization on carbon nanotubes via a two-step process of diimide-activated amidation. *JOURNAL OF MATERIALS CHEMISTRY*, 14(1):37–39, 2004.

[84] ET Mickelson, CB Huffman, AG Rinzler, RE Smalley, RH Hauge, and JL Margrave. Fluorination of single-wall carbon nanotubes. *CHEMICAL PHYSICS LETTERS*, 296(1-2):188–194, OCT 30 1998.

[85] E Unger, A Graham, F Kreupl, M Liebau, and W Hoenlein. Electrochemical functionalization of multi-walled carbon nanotubes for solvation and purification. *CURRENT APPLIED PHYSICS*, 2(2):107–111, APR 2002.

[86] K Esumi, M Ishigami, A Nakajima, K Sawada, and H Honda. Chemical treatment of carbon nanotubes. *CARBON*, 34(2):279–281, 1996.

[87] RQ Yu, LW Chen, QP Liu, JY Lin, KL Tan, SC Ng, HSO Chan, GQ Xu, and TSA Hor. Platinum deposition on carbon nanotubes via chemical modification. *CHEMISTRY OF MATERIALS*, 10(3):718–722, MAR 1998.

[88] ML Sham and JK Kim. Surface functionalities of multi-wall carbon nanotubes after UV/Ozone and TETA treatments. *CARBON*, 44(4):768–777, APR 2006.

[89] Peng Cheng Ma, Jang-Kyo Kim, and Ben Zhong Tang. Functionalization of carbon nanotubes using a silane coupling agent. *CARBON*, 44(15):3232–3238, DEC 2006.

[90] S. C. Wang, K. S. Chang, and C. J. Yuan. Enhancement of electrochemical properties of screen-printed carbon electrodes by oxygen plasma treatment. *ELECTROCHIMICA ACTA*, 54(21):4937–4943, AUG 30 2009.

[91] Nanjundan Ashok Kumar In-Yup Jeon, Dong Wook Chang and Jong-Beom Baek. *Carbon Nanotubes - Polymer Nanocomposites*. InTech, 2011.

[92] Fan WenJie and Zhang RuiQin. Structural and electronic properties of single-walled carbon nanotubes adsorbed with 1-pyrenebutanoic acid, succinimidyl ester. *SCIENCE IN CHINA SERIES B-CHEMISTRY*, 51(12):1203–1210, DEC 2008. 10th National Conference on Quantum Chemistry, Nanjing, PEOPLES R CHINA, MAY 31-JUN 02, 2008.

[93] Liangmin Zhang, Jacquelyn Thomas, Susan D. Allen, and You-Xiong Wang. Optical power limiting and nonlinear absorption effects of polymer functionalized carbon nanotube thin films. *OPTICAL ENGINEERING*, 49(6), JUN 2010.

[94] B Mc Carthy, JN Coleman, R Czerw, AB Dalton, DL Carroll, and WJ Blau. Microscopy studies of nanotube-conjugated polymer interactions. *SYNTHETIC METALS*, 121(1-3, SI):1225–1226, MAR 15 2001. 16th International Conference on Science and Technology of Synthetic Metals (ICSM 2000), GASTEIN, AUSTRIA, JUL 15-21, 2000.

[95] DE Hill, Y Lin, AM Rao, LF Allard, and YP Sun. Functionalization of carbon nanotubes with polystyrene. *MACROMOLECULES*, 35(25):9466–9471, DEC 3 2002.

[96] Linda Vaisman, H. Daniel Wagner, and Gad Marom. The role of surfactants in dispersion of carbon nanotubes. *ADVANCES IN COLLOID AND INTERFACE SCIENCE*, 128:37–46, DEC 21 2006.

[97] QH Zhang, S Rastogi, DJ Chen, D Lippits, and PJ Lemstra. Low percolation threshold in single-walled carbon nanotube/high density polyethylene composites prepared by melt processing technique. *CARBON*, 44(4):778–785, APR 2006.

[98] MF Islam, E Rojas, DM Bergey, AT Johnson, and AG Yodh. High weight fraction surfactant solubilization of single-wall carbon nanotubes in water. *NANO LETTERS*, 3(2):269–273, FEB 2003.

[99] RJ Chen, S Bangsaruntip, KA Drouvalakis, NWS Kam, M Shim, YM Li, W Kim, PJ Utz, and HJ Dai. Noncovalent functionalization of carbon nanotubes for highly specific electronic biosensors. *PROCEEDINGS OF THE NATIONAL ACADEMY OF SCIENCES OF THE UNITED STATES OF AMERICA*, 100(9):4984–4989, APR 29 2003.

[100] F. Ostendorf, C. Schmitz, S. Hirth, A. Kuehnle, J. J. Kolodziej, and M. Reichling. How flat is an air-cleaved mica surface? *NANOTECHNOLOGY*, 19(30), JUL 30 2008.

[101] H SEIDEL, L CSEPREGI, A HEUBERGER, and H BAUMGARTEL. ANISOTROPIC ETCHING OF CRYSTALLINE SILICON IN ALKALINE-SOLUTIONS .1. ORIENTATION DEPENDENCE AND BEHAVIOR OF PASSIVATION LAYERS. *JOURNAL OF THE ELECTROCHEMICAL SOCIETY*, 137(11):3612–3626, NOV 1990.

[102] Olli Herranen. Combined electrical transport and raman measurements of individual single-walled carbon nanotubes. Master's thesis, University of Jyvaskyla, 2009.

[103] http://www4.nau.edu/microanalysis/microprobe-sem/signals.html.

[104] http://www.globalsino.com/em/page4603.html.

[105] Dr. Michael D.G. Steigerwald. New detection system for leo fe-sem, ultra low voltage bse imaging.

[106] VP Hytonen, JAE Maatta, TKM Nyholm, O Livnah, Y Eisenberg-Domovich, D Hyre, HR Nordlund, J Horha, EA Niskanen, T Paldanius, T Kulomaa, EJ Porkka, PS Stayton, OH Laitinen, and MS Kulomaa. Design and construction of highly stable, protease-resistant chimeric avidins. *JOURNAL OF BIOLOGICAL CHEMISTRY*, 280(11):10228–10233, MAR 18 2005.

[107] Richard P. Feynman. There's plenty of room at the bottom: an invitation to enter a new field of physics. Technical report, CalTech, 1959.

[108] KE DREXLER. MOLECULAR ENGINEERING - AN APPROACH TO THE DEVELOPMENT OF GENERAL CAPABILITIES FOR MOLECULAR MANIPULATION. *PROCEEDINGS OF THE NATIONAL ACADEMY OF SCIENCES OF THE UNITED STATES OF AMERICA-PHYSICAL SCIENCES*, 78(9):5275–5278, 1981.

[109] JM Lehn. Toward complex matter: Supramolecular chemistry and self-organization. *PROCEEDINGS OF THE NATIONAL ACADEMY OF SCIENCES OF THE UNITED STATES OF AMERICA*, 99(8):4763–4768, APR 16 2002.

[110] S.R.Elliott. *The Physics and Chemistry of Solids*. John Wiley & Sons, 1998.

[111] C BUSTAMANTE and D KELLER. SCANNING FORCE MICROSCOPY IN BIOLOGY. *PHYSICS TODAY*, 48(12):32–38, DEC 1995.

[112] R Sharma. An environmental transmission electron microscope for in situ synthesis and characterization of nanomaterials. *JOURNAL OF MATERIALS RESEARCH*, 20(7):1695–1707, JUL 2005.

[113] G BINNIG, CF QUATE, and C GERBER. ATOMIC FORCE MICROSCOPE. *PHYSICAL REVIEW LETTERS*, 56(9):930–933, MAR 3 1986.

[114] FJ GIESSIBL. ATOMIC-RESOLUTION OF THE SILICON (111)-(7X7) SURFACE BY ATOMIC-FORCE MICROSCOPY. *SCIENCE*, 267(5194):68–71, JAN 6 1995.

[115] A. Cricenti, S. Colonna, M. Girasole, P. Gori, F. Ronci, G. Longo, S. Dinarelli, M. Luce, M. Rinaldi, and M. Ortenzi. Scanning probe microscopy in material science and biology. *JOURNAL OF PHYSICS D-APPLIED PHYSICS*, 44(46), NOV 23 2011.